ANALYSIS OF FUNCTIONAL MAGNETIC RESONANCE IMAGING DATA USING SIGNAL PROCESSING TECHNIQUES

A Thesis

Submitted to the Faculty

of

Purdue University

by

Sea Chen

In Partial Fulfillment of the

Requirements for the Degree

of

Doctor of Philosophy

December 2002

To my parents and Abigail.

ACKNOWLEDGMENTS

I would like express my sinceress debt of gratitude to my major advisors, Prof. Charles A. Bouman and Prof. Mark J. Lowe. Their tireless effort, strong commitment to this collaborative body of work, and expert guidance have enriched my academic career and my life beyond what I could ever have hoped to imagine. Thank you for being so generous with your time and patience.

I would also like to thank my parents. Without their encourangement and endless toil, the opportunities for this journey would be lost to me. Thank you for providing everything I ever needed to undertake my dreams.

I want to thank Abigail for being there every step of the way. The everyday emotional support she that provides keeps me going. Thank you for giving so much of yourself, with so much love and patience.

I would like to thank my committee members Prof. Peter C. Doerschuk and Prof Edward J. Delp for their suggestions and comments. I would like to thank Prof. Doerschuk specifically for all the career and academic advice he has provide me since my undergraduate days. My thanks also go out to Prof. George Wodicka, Mary Debruicker, and Dr. William Bosron for facilitating my transit through the program and to Prof. Nicholas Peppas and the NSF-IGERT PTDD program for providing the funding opportunities in my first 2 years. I would also like to thank Dr. Mario Dzemidzic, Dr. Pallab Bhattacharyya, Dr. Joseph Lurito, Dr. Micheal Phillips, Dr. Vince Matthews, and Julie Lowe from the Division of Imaging Sciences for their advice and support. Lastly, I would like to thank all my friends who have helped me along the way.

TABLE OF CONTENTS

Page

Page

LIST OF TABLES

LIST OF FIGURES

ABSTRACT

Chen, Sea. Ph.D., Purdue University, December, 2002. Analysis of Functional Magnetic Resonance Imaging Data Using Signal Processing Techniques. Major Professors: Charles A. Bouman and Mark J. Lowe.

The goal of this research was to develop a set of tools for the analysis of functional magnetic resonance imaging data. The study of the blood oxygenation level dependent (BOLD) signal response was specifically targeted.

In the first part of this research, we developed an amplitude independent clustering strategy called clustered components analysis. This technique accounted for activation amplitude variations due to partial volume effects and magnetic field inhomogeneities. The analysis framework also included an automated method for determining the number of clusters based upon the minimum description length criterion. The technique was implemented using the expectation-maximization algorithm.

In the second part of this research, we introduced an analysis method to obtain a high temporal resolution estimate without using a short time-to-repetition (TR). This method that we call supertemporal resolution analysis was developed to reduce the distortion of the BOLD response by blood inflow effects. The technique was based upon maximum a posteriori (MAP) estimation utilizing Bayesian prior model to implement temporal regularization. A crossvalidation strategy was used to automatically determine from the data the level of smoothing. A novel data simulator was developed to test our methods.

1. INTRODUCTION

My research of the past few years was initiated out of a need for better tools to investigate the characteristics of the widely used blood-oxygenation-level-dependent (BOLD) used in functional MRI (fMRI). A widely held assumption in the field of fMRI data analysis was that the BOLD response signal was constant both temporally and spatially. There is no reason to believe this assumption to be true. Firstly, activation amplitude variation due to partial volume effects or magnetic field inhomogeneities is not commonly considered. Secondly, spatial differences in the temporal evolution of the BOLD hemodynamic response are also not commonly considered during signal estimation. Therefore, we used elements of estimation theory to develop signal processing tools to investigate the validity of the assumption and aid in the estimation of the BOLD hemodynamic response.

Much of fMRI research is focused on detection of neuronal activation. However, my research is primarily aimed at studying the temporal evolution characteristics of the hemodynamic response function. Many other research groups are also pursuing this goal with various data analysis methods. Exploratory data driven methods such as independent components analysis, principle components analysis, and fuzzy clustering methods are used quite frequently. Linear systems methods used to deconvolve the hemodynamic impulse response are also often discussed in the literature. Parametric model-based techniques are also quite popular.

Chapter 2 of this thesis describes an data analysis framework called clustered components analysis that utilizes an amplitude independent clustering method on fMRI timeseries data. The data model used to develop the analysis method explicitly included an amplitude factor to account for variations. The estimation scheme described uses the expectation-maximization algorithm to find the maximum likelihood estimates of the cluster timecourses. The technique includes a model order

identification technique based upon the minimum description length criterion. This chapter also introduces a technique for signal subspace estimation to reduce data dimensionality and improve signal to noise ratio as a preprocessing step to clustered components analysis.

Chapter 3 presents a data analysis technique called supertemporal resolution analysis that utilizes the timing characteristics of two-dimensional MR acquisition to find a high temporal resolution estimate of the hemodynamic response signal without using a short time-to-repetition (TR). This technique was developed to combat the distortion of the BOLD response signal by inflow effects when using shorter TR. It is based upon a data model that contains observation matrices for each slice acquired and assumes an identical hemodynamic response signal generating the observed data. The assumption is enforced using the clustered components analysis method presented in the previous chapter. The estimate of the BOLD response is generated using maximum a posteriori estimation utilizing a Bayesian prior that implements temporal regularization. A crossvalidation method is used to find the regularization parameter that governs the smoothness of the estimate. Also presented in this chapter is a novel data simulator used to verify the algorithms.

Chapter 4 outlines suggestions for future work in the extension and improvement of the analysis framework.

2. CLUSTERED COMPONENTS ANALYSIS FOR FMRI

Abstract

A common method of increasing SNR in functional magnetic resonance imaging is to average signal timecourses across voxels. This technique is potentially problematic because the hemodynamic response may vary across the brain. Such averaging may destroy significant features in the temporal evolution of the fMRI response that stem from either differences in vascular coupling to neural tissue or actual differences in the neural response between two averaged voxels. Two novel techniques are presented in this chapter in order to aid in an improved SNR estimate of the hemodynamic response, while preserving statistically significant voxel-wise differences. The first technique is signal subspace estimation for periodic stimulus paradigms that involves a simple thresholding method. This increases SNR via dimensionality reduction. The second technique that we call clustered components analysis (CCA) is a novel amplitude-independent clustering method based upon an explicit statistical data model. It includes an unsupervised method for estimating the number of clusters. Our methods are applied to simulated data for verification and comparison to other techniques. A human experiment was also designed to stimulate different functional cortices. Our methods separated hemodynamic response signals into clusters that tended to be classified according to tissue characteristics.

2.1 Introduction

Functional magnetic resonance imaging (fMRI) has emerged as a useful tool in the study of brain function. This imaging modality utilizes the fact that the MRI signal is sensitive to many of the hemodynamic parameters that change during neuronal

activation (e.g. blood flow, blood volume, oxygenation). The changes in these parameters cause small intensity differences between properly weighted MR images acquired before and during neuronal activation. Although the contrast can be produced by a number of different mechanisms, blood oxygenation level dependent (BOLD) contrast is the method most commonly employed. BOLD contrast is dependent on an decrease in local deoxy-hemoglobin concentration in an area of neuronal activity [1, 2]. This local decrease in paramagnetic material increases the apparent transverse relaxation constant T_2^*, resulting in an increase of MR signal intensity in the area affected. Other methods of functional MR imaging contrast include measurement of cerebral blood flow and volume effects [3]. Although fMRI is widely used, the mechanism of the coupling between brain hemodynamics and neuronal activation is poorly understood.

Although much of the work in fMRI data analysis has revolved around the creation of statistical maps and the detection of activation at different voxel locations [4, 5, 6], there also has been much interest in understanding the BOLD temporal response. Several groups have proposed models relating the various hemodynamic parameters (blood flow, blood volume, hemoglobin concentration, etc.) to the BOLD signal [7, 8]. These models all predict a BOLD temporal response to changing neuronal activity. Verification of the accuracy of these models requires that the predictions be compared to data. However, the low signal-to-noise ratio (SNR) of fMRI measurements typically requires averaging of many voxels in order to achieve a statistically significant result. Thus, the resulting measurement could possibly be a mixture of many different responses. This presents a possible confound in attempts to develop and validate detailed models of the BOLD response.

Some researchers have attempted to address the issue by using parametric methods [9, 10]. The parametric methods usually assume specific signal shapes (Poisson, Gaussian, Gamma, etc.) and attempt to extract the associated parameters for which the data best fit. Others have taken a linear systems approach in which the response is modeled as an impulse response convolved with the stimulus reference function [11, 12]. Exploratory data analysis methods such as principle components analysis

(PCA) [13, 14] and independent components analysis (ICA) [15, 16] are also commonly used by many groups. Recently, clustering methods [17, 18, 19, 20] have become popular as well.

In this chapter, we address the issue of signal averaging by presenting a novel non-parametric clustering method based upon a statistical data model. Specifically, we identify groups of voxels in fMRI data with the same temporal shape, *independent of signal amplitude*. Variations in amplitudes may be due to differences in the concentration of hemodynamic events from partial volume effects or coil geometries. The amplitude variation is explicitly accounted for in our data model. Each distinct response corresponds to a unique *direction* in a multidimensional feature space (see Figure 2.1.

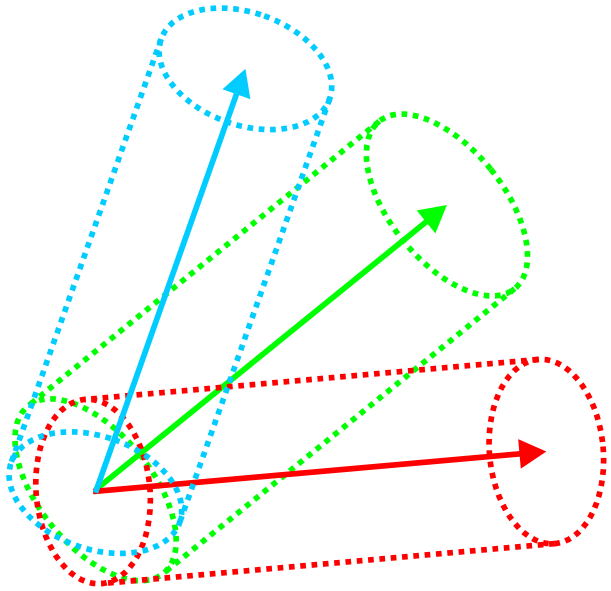

Fig. 2.1. Visualization of cylindrical clusters extracted by CCA. Because CCA finds cluster directions independent of amplitude, the shape of the vector clouds will be cylindrical instead of the more common spherical clouds around class means extracted by other clustering methods.

Our analysis framework is based upon two distinct steps. In the first step, the dimensionality of the voxel timecourses is reduced and feature vectors are obtained. The noise in the feature vectors is then whitened in preparation for the next step.

The second step consists of our novel clustering technique that we call clustered components analysis (CCA).

The dimensionality reduction used in this chapter is similar to the method described by Bullmore, *et al.* [21]. Their method decomposes the temporal response at each voxel into harmonic components corresponding to a sine and cosine series expansion at the appropriate period. We have developed a method to further decrease dimensionality by estimating an M dimensional signal subspace [22]. Although signal subspace estimation (SSE) is not new [23, 24], our method uses a simple thresholding technique and is quite effective. It is implemented by estimating the signal covariance as the positive definite part of the difference between the total signal-plus-noise covariance and the noise covariance. At this point in our analysis technique, each voxel's response is represented by an M dimensional feature vector.

In the second step of our analysis framework, we present a new method for analyzing the multivariate fMRI feature vectors that we call clustered components analysis. This method depends on a explicit data model of the feature vectors and is implemented through maximum likelihood (ML) estimation via the expectation-maximization (EM) algorithm [25, 26]. An agglomerative cluster merging technique based on a minimum description length (MDL) criterion [27] is used to estimate the true number of clusters [28].

Because the truth is not known in a real experiment, synthetic data was generated to test the performance of our method. Other common methods of multivariate data-driven analysis techniques (PCA, ICA, and fuzzy clustering) were applied to the same data set and the results were compared. Finally, a human experiment was performed that stimulated the motor, visual, and auditory cortices. Our methodology was applied to this data. The goal of the human experiment was to produce a set of activation data spanning a broad range of cerebral cortex and a diverse set of neuronal systems. This data set will allow our clustering method to determine the distribution of distinct temporal responses according either to neuronal system or tissue characteristics.

2.2 Theory

2.2.1 Dimensionality Reduction

The first step of our analysis framework is the reduction of dimensionality via decomposition into harmonic components using least squares fitting. This step is similar to that described in [21]. The next step is a novel method of determining the signal subspace by estimating signal and noise covariances and performing an eigendecomposition. The final step is a prewhitening of the noise before application of the clustered components analysis.

Decomposition into Harmonic Components

In a standard block paradigm, control and active states are cycled in a periodic manner during the fMRI experiment. Therefore, the response signal should also be periodic. By assuming periodicity, harmonic components can be used as a basis for decomposition to reduce dimensionality. However, application of the periodicity constraint is not necessary for the technique described in the next section.

The data set of an fMRI experiment, D, can be defined as an $P \times N$ matrix, where N is the number of voxels and P is the number of time points. We first remove the baseline and linear drift components of fMRI data as a preprocessing step [29]. The columns of D are then zero mean, zero drift versions of the voxel timecourses.

The harmonic components, A_l, are a sampling of sines and cosines at the fundamental frequency of the experimental paradigm, γ (in radians/seconds), and its higher harmonics. The number of harmonic components, L, is limited by the requirement that there be no temporal aliasing. In other words, $L < \frac{\Delta t \gamma}{2}$ where Δt is the temporal sampling period.

$$A_l(t) = \begin{cases} \cos\left(\frac{l+1}{2}\gamma t\right) & \text{if } l \text{ odd} \\ \sin\left(\frac{l}{2}\gamma t\right) & \text{if } l \text{ even} \end{cases} \tag{2.1}$$

$$\text{for } l = [1, 2, \cdots, L]$$

We then form a $P \times L$ design matrix

$$A = [a_1, \cdots, a_L]\,, \tag{2.2}$$

where a_l is a column vector formed by sampling the l^{th} harmonic component at the times corresponding to the voxel samples. Using this notation, the data can then be expressed as a general linear model [6] where

$$D = A\Theta + \nu. \tag{2.3}$$

Θ is an $L \times N$ harmonic image matrix containing the linear coefficients, and ν is the $P \times N$ dimensional noise matrix.

Assuming all information in the signal is contained within the range A, an estimate $\hat{\Theta}$ can be computed using a least squares fit, resulting in

$$\hat{\Theta} = (A^t A)^{-1} A^t D \tag{2.4}$$

where the residual error ϵ is given by

$$\begin{aligned} \epsilon &= D - A\hat{\Theta} && (2.5)\\ &= (I - A(A^t A)^{-1} A^t) D && (2.6)\\ &= (I - A(A^t A)^{-1} A^t) \nu\ . && (2.7) \end{aligned}$$

The data set can be expressed in terms of the estimate of the coefficient matrix and the residuals matrix.

$$D = A\hat{\Theta} + \epsilon \tag{2.8}$$

We denote the estimation error as $\tilde{\Theta}$, where

$$\begin{aligned} \tilde{\Theta} &= \hat{\Theta} - \Theta && (2.9)\\ &= (A^t A)^{-1} A^t \nu\ . && (2.10) \end{aligned}$$

Signal subspace estimation

Our next objective is to identify the subspace of the harmonic components that spans the space of all response signals. This signal subspace method improves the signal-to-noise ratio by reducing the dimensionality of the data.

The covariance matrices for the signal, signal-plus-noise, and the noise are defined by the following relations.

$$\begin{aligned} R_s &= \frac{1}{N} E\left[\Theta\Theta^t\right] \\ R_{sn} &= \frac{1}{N} E\left[\hat{\Theta}\hat{\Theta}^t\right] \\ R_n &= \frac{1}{N} E\left[\tilde{\Theta}\tilde{\Theta}^t\right] \end{aligned}$$

Since we can not observe Θ directly, we must first estimate R_{sn} and R_n, and then use these matrices to estimate R_s. With this in mind, we use the following two estimates for R_{sn} and R_n.

$$\hat{R}_{sn} = \frac{1}{N}\hat{\Theta}\hat{\Theta}^t \tag{2.11}$$

$$\hat{R}_n = \text{trace}\{\epsilon\epsilon^t\}(A^tA)^{-1}/(N(P-L-2)) \ , \tag{2.12}$$

where ϵ is computed using Equation 2.6. The expression for $\hat{R}_n$ is derived in Appendix A.1 using the assumption that the noise ν is white and is shown to be an unbiased estimate for R_n. Note that the denominator of the expression reflects the reduction in degrees of freedom when the 2 nuisance components are removed. Since $\hat{R}_{sn}$ and $\hat{R}_n$ are both unbiased estimates of the true covariances, we may form an unbiased estimate of the signal covariance R_s as

$$\hat{R}_s = \hat{R}_{sn} - \hat{R}_n \ . \tag{2.13}$$

The corresponding eigendecomposition is then

$$\hat{R}_s = U_s \Lambda_s {U_s}^t. \tag{2.14}$$

Generally, the eigenvalues of $\hat{R}_s$ will all be non-zero due to noise in the estimation process, so the corresponding signal subspace will have dimension L. However, the

dimensionality of the subspace can be reduced by exploiting the fact that R_s must have positive eigenvalues because it is a covariance matrix. We apply this constraint by forming a new $M \times M$ diagonal matrix $\hat{\Lambda}_s$, which contains only the M positive diagonal elements in Λ_s.

Only the columns of U_s corresponding to the positive eigenvalues in Λ_s are retained, yielding the $L \times M$ modified eigenvector matrix $\hat{U}_s$. The reduced dimension signal component, or eigenimage, can then be written as

$$\hat{Y} = \hat{U}_s^t \hat{\Theta}. \tag{2.15}$$

The eigenimage $\hat{Y}$ contains the linear coefficients for the eigensequences $\Sigma = A\hat{U}_s$.

The clustered components analysis presented in the following section assumes that the noise is white. Therefore, we apply a whitening filter W to form

$$Y = W\hat{Y} \tag{2.16}$$

as described in Appendix A.2. The column vectors of Y correspond to M dimensional feature vectors that describe the timecourse of each voxel. The timecourse realizations of the individual voxels may be reconstructed via the following relation.

$$\hat{D} = \Sigma W^{-1} Y \tag{2.17}$$

2.2.2 Clustered Component Analysis

The method of clustered components analysis is developed in this section. The goal of the method is to cluster voxels into groups that represent similar shapes and to estimate the representative timecourses. Specifically, we apply the analysis to the feature vectors Y found in Equation 2.16. The analysis not only allows for the estimation of cluster timecourses, but also estimates the total number of clusters automatically. The algorithm consists of two steps. The first step is the estimation of the timecourses using the expectation-maximization algorithm. Estimation of the number of clusters occurs in the second step using the minimum description length criterion. See Figure 2.2 for a summary of the CCA algorithm.

Data model

Let Y_n be the n^{th} column of the matrix Y found in Equation 2.16. Y_n is a vector of parameters specifying the timecourse or the M dimensional feature vector for voxel n. Furthermore, let $E_K = [e_1, \cdots, e_K]$ be the K zero mean, zero drift component directions (representing K clusters) in the feature space, each with unit norm (${e_k}^t e_k = 1, \forall k \in [1, 2, \cdots, K]$). The basic data model can be written as

$$Y_n = \alpha_n e_{x_n} + \omega_n \ , \tag{2.18}$$

where α_n is the unknown amplitude for voxel n, $1 \leq x_n \leq K$ is the class of the voxel, and ω_n is zero mean, Gaussian noise.

Because the data have been whitened, we assume that $E[\omega_n \omega_n^t] = I$. The probability density function of the voxel n can be stated as

$$p_{y_n|x_n}(y_n|k, E_K, \alpha_n) = \frac{1}{(2\pi)^{(M-1)/2}} \exp\left\{-\frac{1}{2}(y_n - \alpha_n e_k)^t (y_n - \alpha_n e_k)\right\}, \tag{2.19}$$

with log-likelihood function being

$$\log p_{y_n|x_n}(y_n|k, E_K, \alpha_n) = -\frac{M-1}{2}\log 2\pi - \frac{1}{2}(y_n^t y_n - 2\alpha_n y_n^t e_k + \alpha_n^2). \tag{2.20}$$

In order to resolve the dependence on the unknown amplitude, the maximum likelihood estimate $\hat{\alpha}_n$ of the amplitude is found.

$$\begin{aligned} \hat{\alpha}_n &= \underset{\alpha_n}{\text{argmax}}\{\log p_{y_n|x_n}(y_n|k, E_K, \alpha_n)\} \\ &= {y_n}^t e_k \end{aligned} \tag{2.21}$$

The amplitude estimate in Equation 2.21 is then substituted into the log-likelihood of Equation 2.20.

$$\log p_{y_n|x_n}(y_n|k, E_K, \hat{\alpha}_n) = -\frac{M-1}{2}\log 2\pi - \frac{1}{2}\left(y_n^t y_n - {e_k}^t y_n {y_n}^t e_k\right) \tag{2.22}$$

From Equation 2.22, the density function may be written as

$$p_{y_n|x_n}(y_n|k, E_K, \hat{\alpha}_n) = \frac{1}{(2\pi)^{(M-1)/2}} \exp\left\{-\frac{1}{2}\left(y_n^t y_n - {e_k}^t y_n {y_n}^t e_k\right)\right\}. \tag{2.23}$$

The class of voxel n is specified by the class label x_n, which is an independent, identically distributed discrete random variable taking on integer values from 1 to K. We define $\pi_k = P\{X_n = k\}$ as the prior probabilities that a voxel is of class k. The set of prior probabilities for K classes are then defined to be $\Pi_K = [\pi_1, \cdots, \pi_K]$, where $\sum_{k=1}^{K} \pi_k = 1$.

Using Bayes rule, the voxel probability density can be written without conditioning on class label.

$$p_{y_n}(y_n|K, E_K, \Pi_K, \hat{\alpha}_n) = \sum_{k=1}^{K} p_{y_n|x_n}(y_n|k, E_K, \hat{\alpha}_n)\pi_k \tag{2.24}$$

$$= \sum_{k=1}^{K} \left(\frac{1}{(2\pi)^{(M-1)/2}} \exp\left\{ -\frac{1}{2}\left(y_n^t y_n - {e_k}^t y_n {y_n}^t e_k \right) \right\} \right) \pi_k \tag{2.25}$$

We note that this is a Gaussian mixture distribution [30].

The log-likelihood is then calculated for the whole set of voxels.

$$\log p_y(y|K, E_K, \Pi_K, \hat{\alpha}) = \sum_{n=1}^{N} \log \left(\sum_{k=1}^{K} p_{y_n|x_n}(y_n|k, E_K, \hat{\alpha}_n)\pi_k \right)$$

$$= \sum_{n=1}^{N} \log \left[\sum_{k=1}^{K} \left(\frac{1}{(2\pi)^{(M-1)/2}} \exp\left\{ -\frac{1}{2}\left(y_n^t y_n - {e_k}^t y_n {y_n}^t e_k \right) \right\} \pi_k \right) \right] \tag{2.26}$$

Parameter estimation using the expectation-maximization algorithm

The aim of this section is to estimate the parameters E_K and Π_K in the data model. This is done by finding the maximum likelihood estimates for the log-likelihood given in Equation 2.26 for a given cluster number K.

$$(\hat{E}_K, \hat{\Pi}_K) = \underset{E_K, \Pi_K}{\operatorname{argmax}} \log p_y(y|K, E_K, \Pi_K, \hat{\alpha}) \tag{2.27}$$

The maximum likelihood estimates $\hat{E}_K$ and $\hat{\Pi}_K$ in Equation 2.27 are found by using the expectation-maximization algorithm [25, 30].

In order to compute the expectation step of the EM algorithm, we must first compute the posterior probability that each voxel label x_n is of class k.

$$p_{x_n|y_n}(k|y_n, K, E_K, \Pi_K, \hat{\alpha}_n) = \frac{p_{y_n|x_n}(y_n|k, E_K, \hat{\alpha}_n)\pi_k}{\sum_{l=1}^{K} p_{y_n|x_n}(y_n|k, E_K, \hat{\alpha}_n)\pi_l} \tag{2.28}$$

In the expectation step of the EM algorithm, the estimated number of voxels per class $\bar{N}_{k|K}^{(i)}$ and the estimated covariance matrix of the class $\bar{R}_{k|K}^{(i)}$ given the current estimation of the parameters ${E_K}^{(i)}$ and ${\Pi_K}^{(i)}$ must be computed. See Appendix A.3.1 for more details. Because the EM algorithm is iterative, the superscripts (i) denote iteration number. The subscript $k|K$ denotes the parameter corresponding to the k^{th} cluster out of a total of K clusters.

$$\bar{N}_{k|K}^{(i)} = \sum_{n=1}^{N} p_{x_n|y_n}(k|y_n, {E_K}^{(i)}, {\Pi_K}^{(i)}, \hat{\alpha}_n) \tag{2.29}$$

$$\bar{R}_{k|K}^{(i)} = \frac{1}{\bar{N}_{k|K}^{(i)}} \sum_{n=1}^{N} y_n y_n^t \, p_{x_n|y_n}(k|y_n, {E_K}^{(i)}, {\Pi_K}^{(i)}, \hat{\alpha}_n) \tag{2.30}$$

In the maximization step of the EM algorithm, the parameters are reestimated from the values found in the expectation step (see Equation 2.29 and Equation 2.30, yielding ${E_K}^{(i+1)}$ and ${\Pi_K}^{(i+1)}$. Let $e_{max}\{R\}$ be the principle eigenvector of R.

$$e_k^{(i+1)} = e_{max}\{\bar{R}_{k|K}^{(i)}\} \tag{2.31}$$

$$\pi_k^{(i+1)} = \bar{N}_{k|K}^{(i)}/N \tag{2.32}$$

for $k \in [1, 2, \cdots, K]$ (see Appendix A.3.2 for more details).

Equation 2.31 and Equation 2.32 are alternately iterated with Equation 2.29 and Equation 2.30 (using Equation 2.28. The iterations are stopped when the difference in the log-likelihood (see Equation 2.26 for subsequent iterations is less than an arbitrary stopping criterion, υ. We then denote the final estimates of the parameters for a given number of clusters K as $\hat{E}_K$ and $\hat{\Pi}_K$.

Model order identification

Our objective is not only to estimate the component vectors $\hat{E}_K$ and the prior probabilities $\hat{\Pi}_K$ from observations, but also to estimate the number of classes $\hat{K}$. We use the minimum description length (MDL) criterion developed by Rissanen [27], which incorporates a penalty term $KM\log(NM)/2$. The term NM represents the

number of scalar values required to represent the data, and the term KM represents the number of scalar parameters encoded by $\hat{E}_K$ and $\hat{\Pi}_K$.

$$MDL(K, E_K, \Pi_K) = -\log p_y(y|K, E_K, \Pi_K, \hat{\alpha}) + \frac{1}{2} KM \log(NM) \tag{2.33}$$

The MDL criterion is then minimized with respect to K. This is done by starting with K large, and then sequentially merging clusters until $K = 1$. More specifically, for each value of K, the values of $\hat{E}_K$, $\hat{\Pi}_K$, and $MDL(K, \hat{E}_K, \hat{\Pi}_K)$ are calculated using the EM algorithm from Section 2.2.2. Next, the two most similar clusters are merged, K is decremented to $K-1$, and the process is repeated until $K = 1$. Finally, we select the value of $\hat{K}$ (and corresponding parameters $\hat{E}_{\hat{K}}$ and $\hat{\Pi}_{\hat{K}}$) that resulted in the smallest value of the MDL criterion.

This merging approach requires that we define a method for selecting similar clusters. For this purpose, we define the following distance function between the clusters l and m

$$d(l, m) = \sigma_{max}(\bar{R}_{l|K}) + \sigma_{max}(\bar{R}_{m|K}) - \sigma_{max}(\bar{R}_{l|K} + \bar{R}_{m|K}) \tag{2.34}$$

where $\sigma_{max}(R)$ denotes the principal eigenvalue of R. In Appendix A.4 we show that this distance function is an upper bound on the change in the MDL value (see Equation A.21). Therefore, by choosing the two clusters $\hat{l}$ and $\hat{m}$ that minimize the cluster distance,

$$(\hat{l}, \hat{m}) = \underset{l,m}{\operatorname{argmin}}\, d(l, m) \tag{2.35}$$

we minimize an upper bound on the resulting MDL criterion. The parameters of the new cluster formed by merging $\hat{l}$ and $\hat{m}$ are given by

$$\pi_{(\hat{l},\hat{m})} = \pi_{\hat{l}} + \pi_{\hat{m}} \tag{2.36}$$

$$e_{(\hat{l},\hat{m})} = e_{max}\{\bar{R}_{\hat{l}|K} + \bar{R}_{\hat{m}|K}\}\ . \tag{2.37}$$

The remaining cluster parameters stay constant, and the merged parameters then become the initial parameters for the iterations of the EM algorithm used to find estimates for $K - 1$ clusters.

To start the algorithm, a large number of clusters K_0 is chosen. Then, the parameters ${E_{K_0}}^{(1)}$ and ${\Pi_{K_0}}^{(1)}$ are initialized for each class $\{k : k = 1, 2, \cdots, K_0\}$ by Equation 2.38, Equation 2.39, and Equation 2.40. The initial priors are chosen such that classes are equally distributed. The initial component directions are chosen such that they all fall along the principle eigenvector of the estimated data covariance matrix given in Equation 2.40.

$$\pi_k^{(1)} = \frac{1}{K_0} \tag{2.38}$$

$$e_k^{(1)} = e_{max}\{\bar{R}_{k|K}^{(1)}\} \tag{2.39}$$

where

$$\bar{R}_{k|K}^{(1)} = \frac{1}{N}\sum_{n=1}^{N} y_n y_n^t \tag{2.40}$$

2.3 Methods

2.3.1 Experimental paradigm

An experimental paradigm was designed to activate the auditory, visual, and motor cortices. The paradigm was arranged so all activation occurred in sync at a cycle length of 64 seconds: 32 seconds control, 32 seconds active. The timing of the paradigm was as follows: 16 seconds lead in (control), 4 cycles of the paradigm (4 x 64 seconds), 32 seconds control, and 16 seconds lead out (control). See Figure 2.3 for a diagram of paradigm timing. The visual cortex was activated using a flashing 8Hz checkerboard pattern (6×8 squares) with a blank screen control state viewed through fiber-optic goggles (Avotec, Inc., Stuart, FL). The flashing checkerboard was shown to provide robust activation throughout the visual system [31]. The auditory cortex was activated using backwards speech through pneumatic headphones (Avotec). The backwards speech was shown to provide robust activation in the primary auditory cortex [32]. Auditory control was silence through the headphones (note that the ambient scanner noise is heard by the subject throughout the scan). The visual and auditory stimuli were constructed using commercial software (Adobe AfterEffects,

initialize K to K_0

initialize ${E_{K_0}}^{(1)}$ and ${\Pi_{K_0}}^{(1)}$ using Equation 2.38, Equation 2.39, and Equation 2.40

while $K > 1$

$i \leftarrow 1$

do

compute the posterior probabilities $p_{x_n|y_n}(k|y_n, K, E_K, \Pi_K, \hat{\alpha_n})$ for all n using Equation 2.28

E-step: compute $\bar{N}_{k|K}^{(i)}$ and $\bar{R}_{k|K}^{(i)}$ using Equation 2.29 and Equation 2.30

M-step: compute $E_K^{(i+1)}$ and $\Pi_K^{(i+1)}$ using Equation 2.31 and Equation 2.32

$\delta \leftarrow \log p_y(y|K, {E_K}^{(i+1)}, {\Pi_K}^{(i+1)}, \hat{\alpha}) - \log p_y(y|K, {E_K}^{(i)}, {\Pi_K}^{(i)}, \hat{\alpha})$

$i \leftarrow i + 1$

while $\delta > \upsilon$ (where υ is the stopping tolerance)

set $\hat{E}_K = {E_K}^{(i)}$ and $\hat{\Pi}_K = {\Pi_K}^{(i)}$

compute $MDL_K = MDL(K, \hat{E}_K, \hat{\Pi}_K)$ using Equation 2.33

save $\hat{E}_K$ and $\hat{\Pi}_K$ and MDL_K

find the two clusters $\hat{l}$ and $\hat{m}$ which minimize the distance function $d(l, m)$ using Equation 2.34 and Equation 2.35

merge clusters l and m to form ${E_{K-1}}^{(1)}$ and ${\Pi_{K-1}}^{(1)}$ using Equation 2.36 and Equation 2.37

$K \leftarrow K - 1$

end

choose $\hat{K}$ and the corresponding $\hat{E}_{\hat{K}}$ and $\hat{\Pi}_{\hat{K}}$ which minimize the MDL

Fig. 2.2. Summary of clustered components analysis

Adobe Systems, Inc., San Jose, CA). The motor cortex was activated through a complex finger-tapping task. Left and right fingers were placed opposed in a mirror-like fashion in the rest position and tapped together in a self paced way in the following pattern for activation: thumb, middle, little, index, ring, repeat. This complex finger-tapping task was shown to provide robust motor cortex activation [33]. Tapping was cued by the onset of visual and auditory stimuli. Rest was the control state for the motor paradigm.

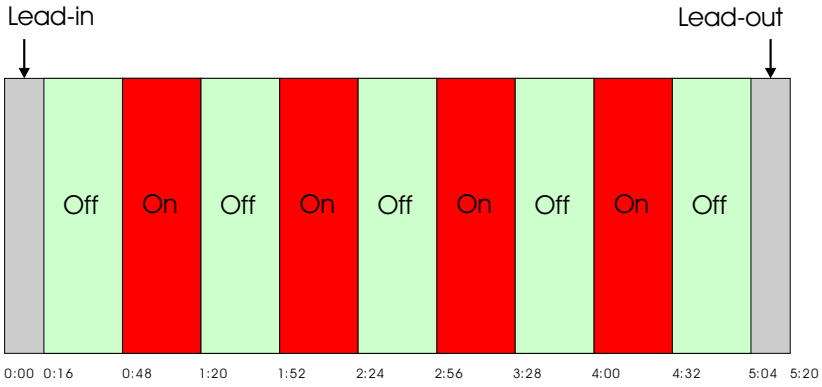

Fig. 2.3. Experimental paradigm timing

2.3.2 Human data acquisition

Whole-brain images of a healthy subject were obtained using a 1.5T GE Echospeed MRI Scanner (GE Medical Systems, Waukeshau, WI). Axial 2D spin echo T_1-weighted anatomic images were acquired for reference with the following parameters: TE = 10ms TR = 500ms, matrix dimensions = 256x128, 15 locations with thickness of 7.0 mm and gap of 2.0 mm covering the whole brain, field-of-view = 24×24 cm.

BOLD-weighted 2D gradient echo echoplanar imaging (EPI) functional images were acquired during a run of the experimental paradigm with the following parameters: TE = 50ms, TR = 2000ms, flip angle = 90^o, matrix dimensions= 64x64, 160 repetitions, and the same locations and field-of-view as the anatomic images.

2.3.3 Synthetic data generation

To test the validity of the our methods, synthetic fMRI images were generated using the averaged functional images gathered from the real data set acquired as per Section 2.3.2 as baseline images. The BOLD response signals were modeled using the methods given by Purdon *et al.* [34], in the three subsequent equations.

The physiologic model is based upon two gamma functions given by

$$g_a(t) = (1 - e^{-1/d_a})^2(t+1)e^{-t/d_a} \tag{2.41}$$

$$g_b(t) = (1 - e^{-1/d_b})e^{-t/d_b}, \tag{2.42}$$

where d_a and d_b are time constants. The activation signal $s(t)$ is then a combination of these gamma functions convolved (denoted by $*$) with the stimulus reference signal $c(t)$ which equals 0 during the control states and 1 during the active states. d_0 denotes a time delay and $f_a, f_b, \text{and} f_c$ are amplitudes which characterize the activation.

$$\begin{aligned} s(t) &= f_a(g_a * c)(t - d_0) + f_b(g_b * c)(t - d_0) + \\ &\quad f_c(g_a * c)(t - d_0)(g_b * c)(t - d_0) \end{aligned} \tag{2.43}$$

The mixture weights, as well as time constant and time delay parameters, were varied between three locations of 8×8 in one slice in order to simulate responses from different functional cortices and/or tissue characteristics. The parameters for Equation 2.41, Equation 2.42, and Equation 2.43 are given in Table 2.1 for each of the signals/locations.

The amplitudes of these signals were modulated by the baseline voxel intensities μ_n using 7% peak activation and then multiplied by a normalized Gaussian window (G) (see Figure 2.4) to simulate the variation in amplitudes across the functional region. Additive white Gaussian noise (ν) was then added to all the voxels at a standard deviation of 2% of the mean baseline voxel intensity in the entire brain.

$$y_n(t) = \mu_n + 0.07\mu_n G_n s_n(t) + \nu_n(t) \tag{2.44}$$

Table 2.1
Parameters used in synthetic data generation

Signal	f_a	f_b	f_c	d_a	d_b	d_0
1	0.6	0.02	0.2	1	10	2
2	0.35	0.2	0.5	3	5	8
3	0.35	0.1	1	5	5	15

2.3.4 Data processing

Synthetic data

In the synthetic data, only the voxels that had been injected with signal were considered for analysis. Mean and drift were removed from the voxel timecourses. Only the timepoints corresponding to the first four cycles were considered (128 out of 160 time points). Because the sequence used was a two-dimensional acquisition, each slice is acquired at staggered timing. Therefore, a different design matrix A was specified for each slice by shifting the harmonic components by the corresponding time delay for the slice. The dimensionality reduction scheme including harmonic decomposition and signal subspace estimation outlined in Section 2.2.1 was performed.

Principle components analysis (PCA) was applied to the synthetic data after harmonic decomposition using the harmonic images $\hat{\Theta}$ given in Equation 2.4. An eigendecomposition was performed on $\hat{R}_{sn}$ given in Equation 2.11 to obtain the principle components. PCA was also applied to the synthetic data after signal subspace estimation. The principle components are the columns of $\hat{U}_s$ derived from Equation 2.14. In both cases, the three principle components were chosen corresponding to the three largest variances.

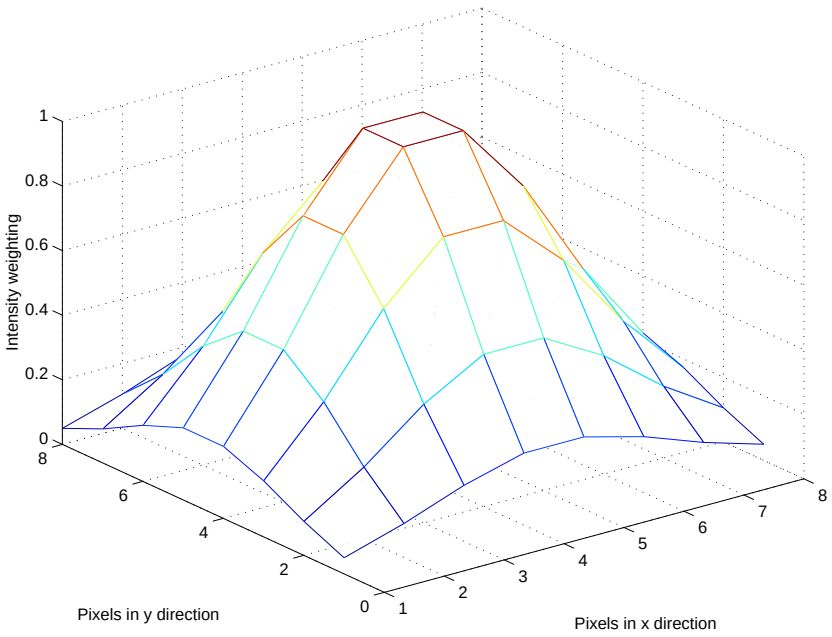

Fig. 2.4. Gaussian window for variation in amplitude in the synthetic data. Each vertex in the mesh corresponds to a voxel in an 8×8 square region of interest. The mesh values at the vertices modulate the amplitudes of activation at the corresponding voxels.

Fuzzy C-means clustering (FCM), using the Matlab fuzzy toolbox (Mathworks, Natick, MA), was also applied to the synthetic data on $\hat{\Theta}$ and unwhitened feature vectors $\tilde{Y}$. The routine was constrained to yield three clusters in both cases.

Spatial independent components analysis, using software available from [35], was applied to $\hat{\Theta}$ and to the $\tilde{Y}$. The analysis was applied unconstrained to yield as many components as channels and also constrained to yield three independent components. For the unconstrained case, the three independent components that best matched (in a least squares sense) the injected signals were chosen.

Clustered components analysis was applied only after signal subspace estimation on the whitened feature vectors Y. The CCA was initialized with $K_0 = 20$ clusters. The resultant estimates were transformed back into the time domain,

$$\tilde{e}_k = \Sigma W^{-1} \hat{e}_k, \forall k \in [1, \cdots, K] \tag{2.45}$$

in a manner similar to Equation 2.17.

Human data

The functional image data were analyzed voxel-by-voxel for evidence of activation using a conventional Student's T-test analysis [29] using in-house software. Regions of interest were drawn on the resulting statistical maps in the cortical regions corresponding to primary activated regions for each of the three stimuli (i.e. precentral gyrus for the motor stimuli, superior temporal gyrus for the auditory stimuli, and the calcarine fissure for the visual stimuli). Only the voxels in the regions of interest were considered in the analysis. The data were processed for the dimensionality reduction in the same manner as the synthetic data. CCA was applied to the resultant feature vectors Y, and the results were transformed back into the time domain using Equation 2.45. CCA for the human data was also initialized with $K_0 = 20$ clusters.

2.4 Results

2.4.1 Synthetic Data

The harmonic decomposition and signal subspace estimation yielded $L = 16$ dimensions for the synthetic data. The resultant signals from PCA, FCM, and ICA applied before and after signal subspace estimation were then least squares fitted to each injected synthetic signal (peak-to-trough amplitude normalized) and were matched by finding the combination with the smallest mean square error per sample. The mean square error results of the analysis methods are shown in Table 2.2. The timesequence realizations are plotted for the analysis methods applied after signal subspace estimation in Figure 2.5.

Hard classification results were then calculated by finding the largest membership value (e.g., largest component for PCA and ICA, largest membership value for FCM, and largest posterior probability for CCA) for each voxel. The number of correct voxel classifications for the analyses is shown in Table 2.3. The hard classification results image for CCA is shown in Figure 2.6.

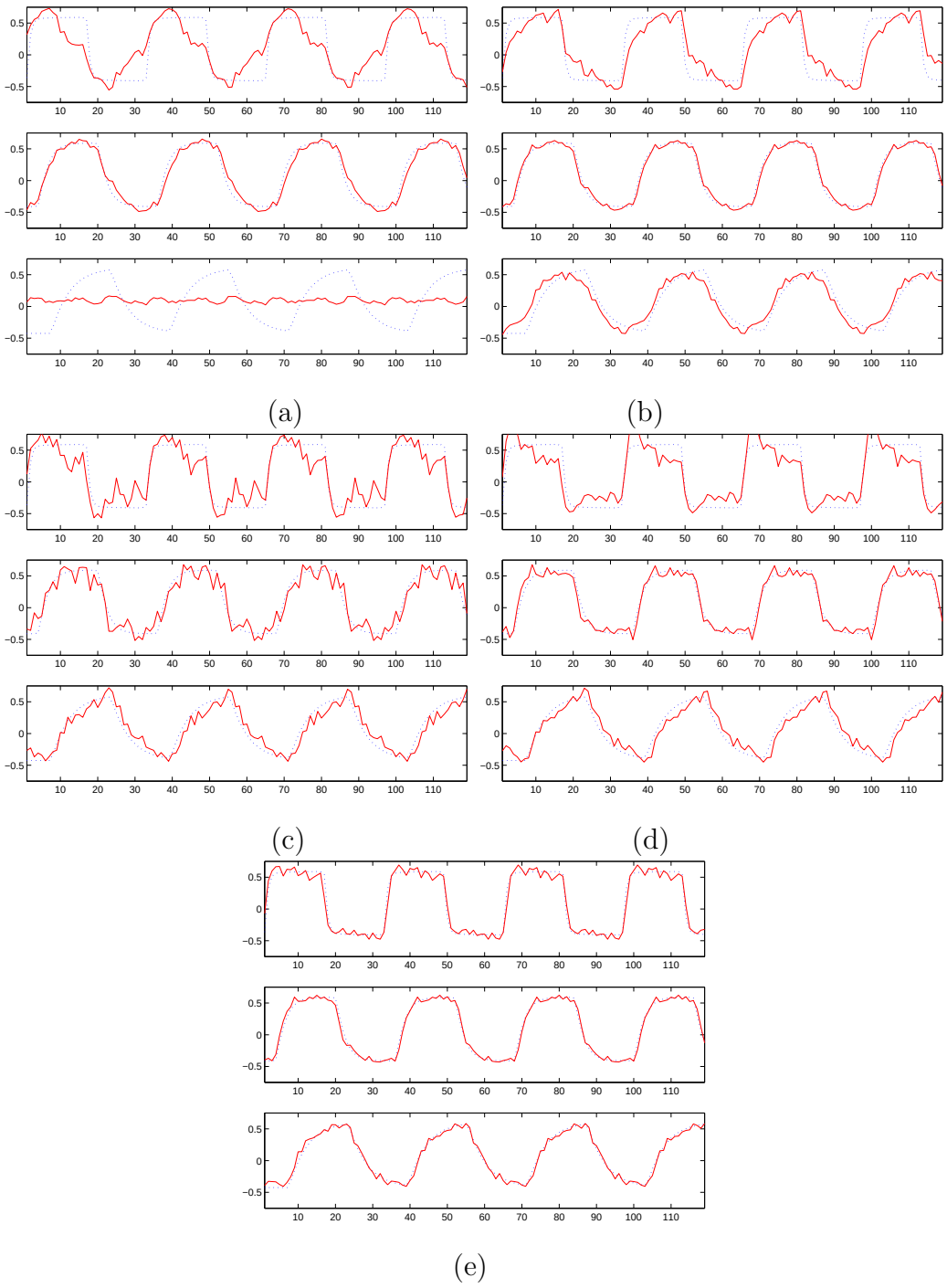

Fig. 2.5. Estimation methods after signal subspace estimation plotted against injected synthetic signal. (a) PCA, (b) FCM, (c) constrained ICA, (d) unconstrained ICA, (e) CCA. The solid blue estimated signals are least squares fitted to the dotted red injected signals.

Table 2.2
Mean squared error for analyses on synthetic data before and after signal subspace estimation (SSE)

	PCA	FCM	ICA (c)	ICA (u)	CCA
Before SSE	5.73×10^{-4}	7.37×10^{-4}	1.02×10^{-3}	2.49×10^{-4}	3.49×10^{-5}
After SSE	5.80×10^{-4}	1.95×10^{-4}	2.21×10^{-4}	1.63×10^{-4}	3.09×10^{-5}

Table 2.3
Number of voxels classified correctly on synthetic data before and after signal subspace estimation (SSE) out of 192 total voxels

	PCA	ICA (c)	ICA (u)	FCM	CCA
Before SSE	61	113	38	95	167
After SSE	111	162	77	151	169

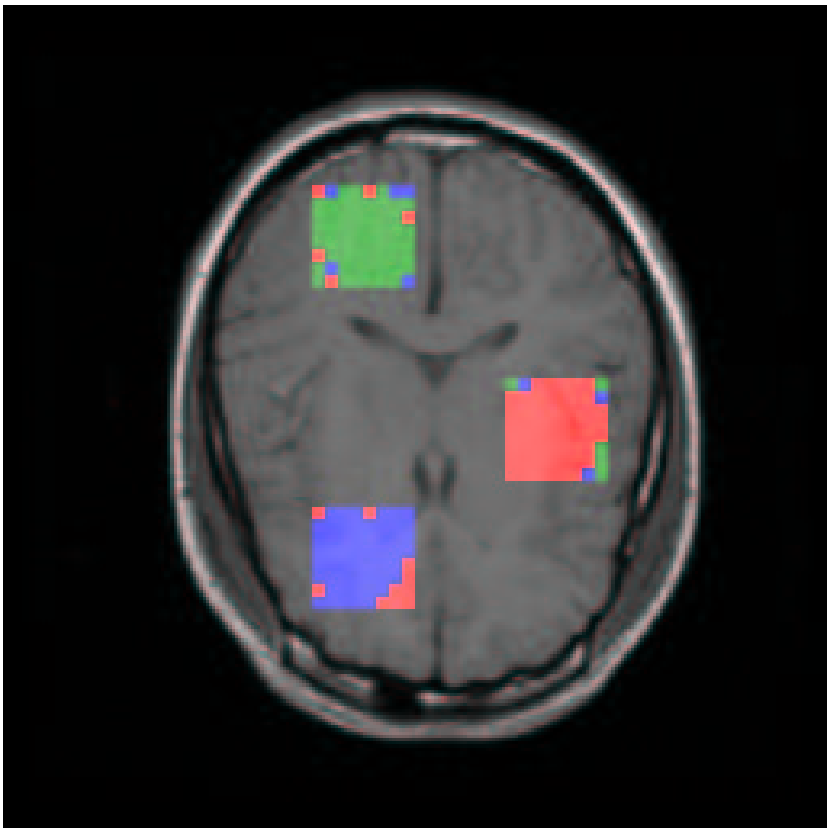

Fig. 2.6. Hard classification results from CCA on synthetic data

2.4.2 Human Data

The signal subspace was found to have $M = 8$ dimensions. CCA returned $\hat{K} = 9$ classes and the components $\hat{E}_9$ from the feature space. The number of voxels in each cluster is displayed in Figure 2.7. The majority of the voxels (94%) lie in the first 5 clusters. The last four clusters contain 10 or less voxels. Therefore, the timesequence realizations of the component directions from the first 5 clusters are given separately from the last 4 clusters in Figure 2.8. Each voxel was then assigned to the class with the highest a posteriori probability. The hard classifications for the first 5 clusters are shown in Figures 2.9 with the accompanying anatomic data. The colors used for the voxels correspond to the class colors in Figure 2.8a.

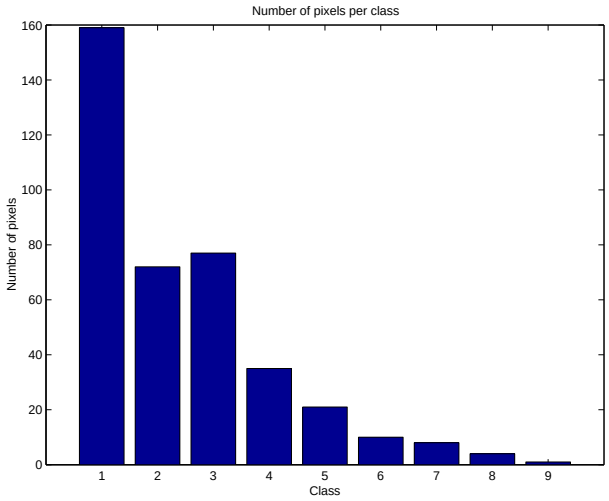

Fig. 2.7. Histogram of the number of voxels in each class for the human data set

2.5 Discussion

2.5.1 Experimental results

Our simulation results show that, as a general rule, mean square error decreased by using signal subspace estimation (except for PCA). The number of voxels classified correctly increased for each analysis method as a result of signal subspace estimation. It can also be seen that CCA outperforms each of the other analysis methods in both mean square error and correct voxel classification. Although in CCA the changes are small before and after signal subspace estimation in both mean square error and correct classification, the signal subspace estimation speeds the algorithm greatly.

The experimental results from the human data reveal that a distinct functional behavior does not correlate directly with each of the functional ROIs, at least for the motor and auditory cortices. Inspection of Figure 2.9 shows that the classes are distributed along patterns of location with respect to sulcal-gyral boundaries. This may reflect that the temporal evolution of the BOLD signal is dependent much more on the vascularization of the tissue than the functional specifics of neuronal activation.

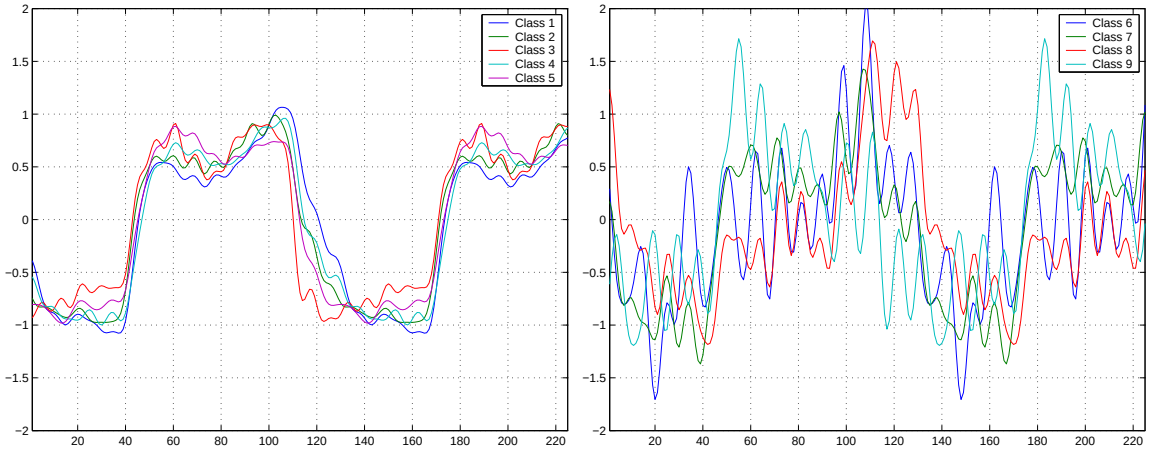

(a) (b)

Fig. 2.8. Timesequence realizations of the feature space for the human data set: (a) timesequences for the first 5 clusters, (b) timesequences for clusters 6-9

2.5.2 Relation to other analysis methods

In this chapter, we have attempted to develop an analysis framework which espouses the advantages of previous methods. This section will detail how our methods relate to other multivariate methods used by other researchers.

Linear time invariant systems methods try to model the hemodynamic impulse response function by using deconvolution. Although it has been shown that for some cases linearity is reasonable [11, 12], for other situations nonlinearities arise [36]. Parametric methods are heavily model driven and not as suitable if data are not described well by the model. Therefore, data-driven methods should be used in fMRI where the mechanisms of the system are unknown. Our approach is data-driven and may be more appropriate in this case.

PCA is a method which uses the eigenanalysis of signal correlations to produce orthogonal components in the directions of maximal variance [37, 38]. However, it is unlikely that the distinct behaviors in fMRI data correspond to orthogonal signals. Backfrieder *et al.* [14], attempted to solve this problem by using an oblique rotation

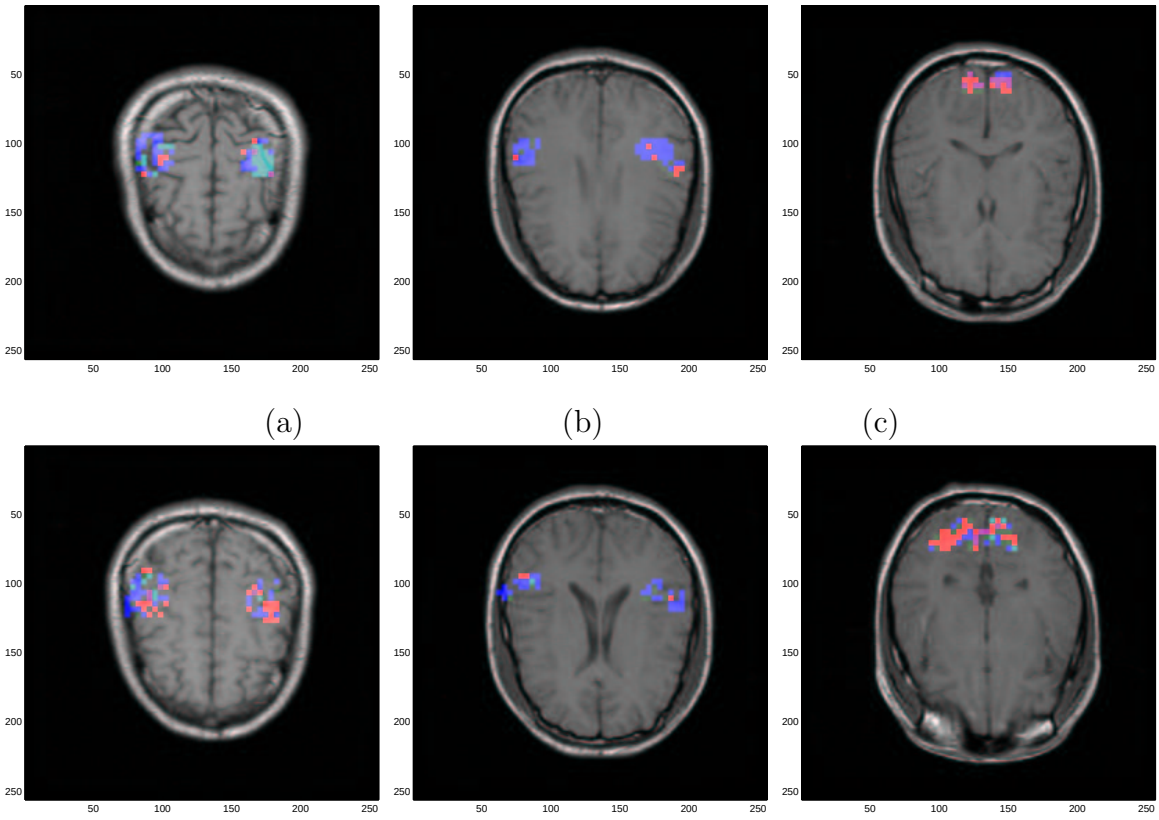

Fig. 2.9. CCA hard classification on the real data set (first 5 clusters). The colors correspond to the class colors shown in Figure 2.8a. (a) upper motor cortex slice, (b) upper auditory cortex slice, (c) - upper visual cortex slice, (d) lower motor cortex slice, (e) lower auditory cortex slice, and (f) - lower visual cortex slice

of the components. Most researchers, however, use PCA as a preprocessing step for dimensionality reduction. A threshold is usually arbitrarily set to the number of components kept [13]. We use a method similar to PCA for dimensionality reduction. Our threshold, however, is determined from the data itself after noise covariance estimation from harmonic decomposition and should effectively remove this subjective aspect the analysis.

ICA is used in signal processing contexts to separate out mixtures of independent sources or invert the effects of an unknown transformation [39]. It was adapted to produce spatial independent components for fMRI datasets by McKeown *et al.* [15, 16]. The fMRI data is modeled as a linear combination of maximally independent (minimally overlapping) spatial maps with component timecourses. It has been pointed out, however, that neuronal dynamics may overlap spatially [40]. Our method does not constrain distinct behaviors to be spatially independent. Another shortcoming of ICA is that it does not lend itself to statistical analysis. McKeown and Sejnowski have attempted to solve this problem by developing a method to calculate the posterior probability of observing a voxel timecourse given the ICA unmixing matrix [41]. Because CCA is based upon an explicit statistical model, it does not suffer from this disadvantage.

Clustering algorithms have been applied to both fMRI raw timecourse data [18, 20, 42] and to timecourse features such as univariate statistics and correlations [43]. Because we are trying to estimate the response signal, we use a hybrid method to characterize the timecourses into lower dimensionality representations. The main problem with most of these clustering methods is that the variation in amplitude is not taken into consideration. Our method produces component *directions* due to the amplitude variances (see Figure 2.1) rather than traditional cluster means. More recently, Brankov *et al.* [44], proposed an alternative clustering approach which is also designed to account for variations in signal amplitude. Another shortcoming of most clustering methods is that the number of clusters is arbitrarily determined. Baune *et al.* [20], attempt to solve this problem by setting a threshold on Euclidean distances

for the merging of clusters. Liang *et al.* [30], also used an information criterion for order identification (AIC and MDL) to analyze PET and SPECT data to find image parameters. Our method uses the MDL criterion plus a cluster merging strategy to determine the number of clusters in an unsupervised manner.

2.5.3 Algorithm details

We use a design matrix A which consists of harmonic components used in the dimensionality reduction applied in this chapter. Periodicity of the response signal is assumed due to the block design of the stimulus paradigm. This assumption allows for the reduction in dimensionality and the estimation of a noise covariance for signal subspace estimation. However, periodicity is not a trait of all stimulus paradigms. In non-periodic paradigm designs, the CCA method can still be applied without the SSE step. It can be seen in Tables 2.2 and 2.3 that CCA performs well even without SSE. Other orthogonal bases, including wavelets and splines, may also be used as the design matrix. These may also allow for estimation of a noise covariance, but we have not explored the details of this approach. CCA can even be applied to event-related approaches where the inter-stimulus interval is random.

In this chapter, the assumption is made that the noise in the images is additive white Gaussian. It is known, in fact, that the noise in magnitude MRI data is Rician [45]. In addition, in dynamic in-vivo MR imaging, physiologic processes introduce correlated "noise." However, as a first order approximation, the additive white Gaussian noise model works fairly well. The framework we have presented can be generalized to more complex noise models.

Because the two steps of our method are both entirely self-sufficient, they can be used independently of each other. The SSE methods of the first step can be used in conjunction with multivariate clustering methods other than our CCA. Conversely, the CCA can be used on any dataset which contain feature vectors which have the

property of amplitude variation which we discussed in Section 2.1. As a generalization, these methods can also be used in applications outside the realm of fMRI.

2.6 Conclusion

In this chapter, we have introduced two novel ideas for the analysis of fMRI time-series data. The first was a method to reduce the dimensionality and increase SNR by using a signal subspace estimation and simple thresholding strategy. The second was the method of clustered components analysis in which the data were iteratively classified independent of signal amplitude. The second method also included a technique to find the number of clusters in an unsupervised manner.

The methodology presented here will allow investigators to improve the estimation of the BOLD signal response by dramatically improving SNR through signal averaging without destroying potentially important statistically distinct temporal elements in the process.

3. SUPERTEMPORAL RESOLUTION ANALYSIS FOR FMRI TIMESERIES DATA

Abstract

Functional MRI (fMRI) has become the tool of choice for investigators studying human brain function. Much research has been concentrated on the detection and localization of the blood-oxygenation-level-dependent (BOLD) signal response within the brain. However, many investigators are now interested in the time evolution of the BOLD response. Temporal resolution is critical in understanding the faster evolving processes in the BOLD response. We have developed novel methods to achieve a high temporal resolution estimate of the BOLD response without the confounding effects of blood inflow that accompany a short time-to-repetition (TR). We have developed a technique called supertemporal resolution (STR) that exploits the slice timing characteristics in two-dimensional echo planar imaging (2D EPI) to obtain a higher sampling rate than the TR. The STR method includes a novel Bayesian prior model within the framework of maximum a posteriori (MAP) estimation to implement temporal regularization. The method uses a crossvalidation strategy to determine the amount of regularization. We have also developed a data simulator based on the balloon model to validate our methods. The simulator uses acquisition parameters to balance BOLD and blood inflow effects in the activation signal. We show that these methods can be used to measure the evolution of the BOLD response without introducing inflow effects that accompany a rapid-sampling approach.

3.1 Introduction

Functional magnetic resonance imaging (fMRI) has become widely used in neuroscientific research. The MRI signal is sensitive to hemodynamic parameters that change during neuronal activation such as blood flow, blood volume, and oxygenation. Therefore, small intensity differences between properly weighted MR images can occur during neuronal activation. Blood-oxygenation-level-dependent (BOLD) contrast is developed in MR images during a decrease in local deoxy-hemoglobin concentration in an area of neuronal activity [1, 2]. Although the BOLD mechanism is the most commonly used method of producing contrast in fMRI, the relationship between the BOLD signal, brain hemodynamics, and neuronal activation is poorly understood.

Much of the research in fMRI data analysis has been centered on the detection and localization of activated voxels [4, 5, 6]. However, there is growing interest in understanding specifics of the BOLD temporal response. For instance, the so-called initial dip is the topic of much debate in the literature [46, 47]. To better understand the faster evolving features of the BOLD response such as the initial dip, an unaliased high temporal resolution estimate is necessary.

A simple way to increase temporal resolution is to sample the data faster. However, using short sample times (time-to-repetition or TR in MR terminology) physically affects the underlying activation signal in two ways. Firstly, the signal-to-noise ratio (SNR) is decreased due to saturation effects because the signal strength is reduced compared to constant noise levels. Secondly, blood inflow effects are more apparent, distorting the BOLD effect. Both physical effects confound the estimation of the BOLD response when using a rapid-sampling approach.

We have developed a method that exploits the slice timing characteristics of two-dimensional (2D) echo planar imaging (EPI) acquisition to obtain a high temporal resolution estimate without using a short TR. Specifically, a temporal resolution as low as the ratio of the TR to the number of slices can be achieved. Our method utilizes the fact that slices in a 2D acquisition are acquired at staggered times. See

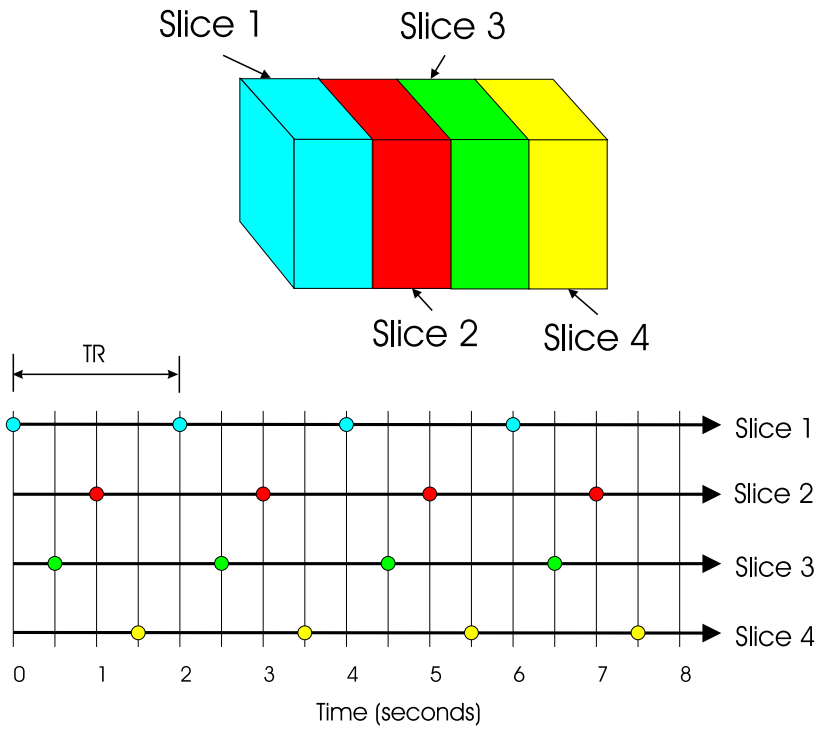

Fig. 3.1. Example of 2D EPI slice timing for four slices. TR is equal to 2 seconds. Note that information is taken every 0.5 seconds.

Figure 3.1 and Table 3.1 for an example of the slice timing for a four slice volume with a TR equal to two seconds. If a set of voxels spanning different slices exhibits the same neuronal behavior (i.e., have the same shape), then the staggered sample times of the different slices will acquire information about the same activation signal at differing times. These ideas are similar to superresolution reconstruction used in image processing to form a high resolution image from several aliased low resolution images [48]. Therefore, a high temporal resolution estimate can be achieved by incorporating slice timing information, even at a long TR.

Our technique, which we call supertemporal resolution (STR) analysis, is based upon maximum a posteriori estimation. We first develop a data model that incorporates slice timing information. The model also considers variable activation amplitude, which is adapted from our Clustered Components Analysis (CCA) method [49]. Temporal regularization is implemented in the STR estimator using a novel Bayesian

Table 3.1
Example of 2D acquisition slice timings for 4 slices and TR = 2 seconds. Note that samples are taken every 0.5 seconds (2 seconds / 4 slices)

Slice #	Sample times (s)
1	0.0, 2.0, 4.0, 6.0, ...
2	0.5, 2.5, 4.5, 6.5, ...
3	1.0, 3.0, 5.0, 7.0, ...
4	1.5, 3.5, 5.5, 7.5, ...

prior model. A crossvalidation strategy [50, 51] is used to determine the amount of regularization necessary.

The STR method requires that the voxels to be analyzed exhibit the same activation signal. We use the CCA method to fulfill this requirement by finding voxel timecourses that exhibit the same shape.

We introduce a data simulator to validate our methods. The simulator uses the balloon model [8] to generate a synthetic BOLD response signal. The data simulator also utilizes acquisition parameters to correctly weight the blood inflow and BOLD effects for differing TRs based upon equations derived by Glover, *et al* [52]. To simulate increases in SNR (as in the case of increasing static field strength), the activation amplitudes are simply multiplied by a factor of 1, 2, 4, 6, or 8. The simulator also incorporates baseline, drift, amplitude, and noise characteristics estimated from human data in the synthetic voxel timecourses. We used the simulator to produce synthetic 4 slice datasets at TR = 2.0 and 0.5 seconds at the various activation amplitudes.

The STR method was applied to the TR = 2.0 second synthetic data, which yielded estimates at 0.5 second temporal resolution. The crossvalidation strategy was evaluated by comparison to the mean square error of the estimates. Two simple estimation methods were also applied to the TR = 0.5 second synthetic data for comparison, also yielding 0.5 second temporal resolution estimates. The first method was a simple averaging of the voxel timecourses. The second method was an averaging

that included the same temporal regularization that was utilized in the STR method. The performance of each method was assessed by comparing the result to the the synthetic BOLD signal generated by the simulator.

The STR method was also applied to data from a human fMRI visual system experiment using 4 slices acquired at at TR = 2.0 seconds. The simple estimation strategies were also applied to human data acquired at TR = 0.5 seconds. Qualitative differences in the results are reported.

3.2 Theory

3.2.1 Data model and the likelihood function

Let y_n be an m-dimensional column vector. This serves as the representation for the timecourse of the n^{th} voxel. Our data model portrays a response in which the shape of the signal is of primary interest, not the amplitude. More specifically, we assume y_n to have the form

$$y_n = \alpha_n \mathbf{A}_{s(n)} e + \omega_n + \psi_n \tag{3.1}$$

where e is the r-dimensional high temporal resolution column vector representing the generating signal behavior, $s(n)$ is the index of the slice that contains the n^{th} voxel, $\mathbf{A}_s$ is the $m \times r$ observation matrix for the s^{th} slice that maps the high resolution timecourse to the observation space and includes slice timing information, α_n is the scalar amplitude for the particular voxel, and ω_n is, without loss of generality, an independent, identically distributed Gaussian $m \times 1$ noise vector with zero mean and variance = 1. The quantity ψ_n is a nuisance vector containing baseline and drift components.

The observation matrices $\mathbf{A}_s$ we subsequently use in this chapter are simple decimation matrices that introduce time shifts corresponding to the slice timing of each voxel n. The rows of these matrices contain all zeros except a one at the appropriate sample time of the particular slice and timepoint. For example, we acquire 4 slices

at TR = 2.0 seconds and use 80 seconds of data (see Figure 3.1 and Table 3.1 for more details). The generating signal is assumed to have a temporal resolution of 0.5 seconds. Therefore, $\mathbf{A}_1$ and $\mathbf{A}_2$ are 40×160 matrices that have the form

$$\mathbf{A}_1 = \begin{pmatrix} 1 & 0 & 0 & 0 & 0 & 0 & 0 & \cdots & 0 & 0 & 0 & 0 & 0 \\ 0 & 0 & 0 & 0 & 1 & 0 & 0 & \cdots & 0 & 0 & 0 & 0 & 0 \\ \vdots & & & & & & & & & & & & \vdots \\ 0 & 0 & 0 & 0 & 0 & 0 & 0 & \cdots & 0 & 1 & 0 & 0 & 0 \end{pmatrix} \tag{3.2}$$

$$\mathbf{A}_2 = \begin{pmatrix} 0 & 1 & 0 & 0 & 0 & 0 & 0 & \cdots & 0 & 0 & 0 & 0 & 0 \\ 0 & 0 & 0 & 0 & 0 & 1 & 0 & \cdots & 0 & 0 & 0 & 0 & 0 \\ \vdots & & & & & & & & & & & & \vdots \\ 0 & 0 & 0 & 0 & 0 & 0 & 0 & \cdots & 0 & 0 & 1 & 0 & 0 \end{pmatrix} . \tag{3.3}$$

In order to construct the likelihood function in a meaningful way, the nuisance vector ψ_n must be removed. We use an $m \times m$ projection matrix $\mathbf{P}$ that is constructed such that $\mathbf{P}\psi_n = 0$ and the other eigenvalues are equal to one. For our example, the projection matrix is given by

$$\mathbf{P} = \mathbf{I}_m - [\vec{1}_m D_m]([\vec{1}_m D_m]^T[\vec{1}_m D_m])^{-1}[\vec{1}_m D_m]^T \ , \tag{3.4}$$

where $\mathbf{I}_m$ is the $m \times m$ identity matrix, $\vec{1}_m$ is an m-dimensional column vector of ones, and D_m is an m-dimensional zero mean linear drift column vector with slope of one. Note that D_m can be generalized into an $m \times k$ matrix where the k columns are basis vectors representing different drifts. Matrix $\mathbf{P}$ projects the data onto a zero-mean, zero-drift subspace. The data model is then

$$\mathbf{P}y_n = \alpha_n \mathbf{P}\mathbf{A}_{s(n)}e + \mathbf{P}\omega_n \ . \tag{3.5}$$

However, since the density function of $\mathbf{P}y_n$ is singular and $\mathbf{P}\omega_n$ is not white, we instead model the density function of $\mathbf{V}y_n$, where $\mathbf{V}$ is an $(m-2) \times m$ orthonormal matrix defined in Equation B.2 of Appendix B.1. The matrix $\mathbf{V}$ contains two less columns

because $\mathbf{P}$ reduces the degrees of freedom by 2. We define $\check{y}_n = \mathbf{V}y_n$, $\tilde{y}_n = \mathbf{P}y_n$, and $\tilde{\mathbf{A}}_s = \mathbf{P}\mathbf{A}_s$. The likelihood function for each voxel is then given by

$$p(\check{y}_n|e,\alpha_n) = \frac{1}{(2\pi)^{\frac{m-2}{2}}} \exp\left(-\frac{1}{2}\left\|\tilde{y}_n - \alpha_n \tilde{\mathbf{A}}_{s(n)} e\right\|^2\right) . \tag{3.6}$$

See Appendix B.1 for more details.

Because the amplitude α_n is unknown, we use the maximum likelihood estimate $\hat{\alpha}_n$, where

$$\hat{\alpha}_n = \frac{\tilde{y}_n^T \tilde{\mathbf{A}}_{s(n)} e}{e^T \tilde{\mathbf{A}}_{s(n)}^T \tilde{\mathbf{A}}_{s(n)} e} . \tag{3.7}$$

After substitution of the amplitude estimate of Equation 3.7 into the likelihood function of Equation 3.6 and simplification, the likelihood function is then expressed independently of amplitude. Note the degrees of freedom is further reduced by 1.

$$p(\check{y}_n|e,\hat{\alpha}_n) = \frac{1}{(2\pi)^{\frac{m-3}{2}}} \exp\left[-\frac{1}{2}\left(\|\tilde{y}_n\|^2 - \left(\frac{\tilde{y}_n^T \tilde{\mathbf{A}}_{s(n)} e}{\left\|\tilde{\mathbf{A}}_{s(n)} e\right\|}\right)^2\right)\right] \tag{3.8}$$

We define the whole set of manipulated timecourses as the vector quantity $\check{y} = (\check{y}_0, \check{y}_1, \cdots, \check{y}_{N-1})^T$, and denote the whole set of estimated amplitudes as the vector $\hat{\alpha} = (\hat{\alpha}_0, \hat{\alpha}_1, \cdots, \hat{\alpha}_{N-1})^T$. We manipulate the likelihood function in Equation 3.8 using the assumption that the voxels are independent and simplify, yielding the log-likelihood for the whole set of voxels given by

$$\begin{aligned} \log p(\check{y}|e,\hat{\alpha}) &= \sum_{n=0}^{N-1} \log p(\check{y}_n|e,\hat{\alpha}_n) \\ &= N \log \frac{1}{(2\pi)^{\frac{m-3}{2}}} - \frac{1}{2}\sum_{n=0}^{N-1} ||\tilde{y}_n||^2 + \frac{1}{2}\sum_{s=0}^{K-1} \frac{e^T \tilde{\mathbf{A}}_s^T \mathbf{R}_s \tilde{\mathbf{A}}_s e}{e^T \mathbf{B}_s e} , \end{aligned} \tag{3.9}$$

where

$$\mathbf{R}_s = \sum_{n\in S} \tilde{y}_n \tilde{y}_n^T , \tag{3.10}$$

$$\mathbf{B}_s = \tilde{\mathbf{A}}_s^T \tilde{\mathbf{A}}_s , \tag{3.11}$$

and $S = \{n : n \in \text{slice } s\}$.

3.2.2 The maximum a posteriori estimate and temporal regularization

We would like to estimate the generating activation signal e using the data model described in the previous section. Maximum a posteriori (MAP) estimation is a common method used for this class of problems. An advantange of using MAP estimation is that known information about the distribution of e can be included using a so-called Bayesian prior.

In our estimation of e, the fact that hemodynamic events tend to be temporally smooth [53] will be utilized. We can impose temporal regularization, or smoothness, on the estimate of e using a Bayesian prior $p(e|\sigma)$, where σ is a parameter that controls the amount of smoothness. A smaller σ indicates more smoothness. The MAP estimate using our data model and a Bayesian prior that imposes temporal regularization can be expressed in the form

$$\hat{e}_\sigma = \underset{e}{\operatorname{argmax}} \{\log p(\check{y}|e, \hat{\alpha}) + \log p(e|\sigma)\} \ . \tag{3.12}$$

Simple Bayesian priors that implement temporal regularization (such as in Tikhonov regularization [54]) are typically used. Some simple priors attempt to capture non-Gaussian aspects of the signal [55, 56]. However, the commonly used priors tend to scale linearly in proportion to the signal and are not well suited to our problem. To avoid this problem, we introduce a new prior adapted from [57] by normalizing with respect to $||e||^p$. In particular, we propose a prior in the form

$$p(e|\sigma) = \frac{1}{Z} \exp\left\{ -\frac{1}{p\sigma^p ||e||^p} \sum_{i=0}^{r-1} (e_i - e_i + 1)^p \right\} \ , \tag{3.13}$$

where Z is a normalizing constant[1].

By incorporating the log-likelihood in Equation 3.9 and the prior in Equation 3.13, we form the explicit STR estimate from Equation 3.12 using MAP estimation.

$$\text{(STR)} \qquad \hat{e}_\sigma = \underset{e}{\operatorname{argmax}} \left\{ \frac{1}{2} \sum_{s=0}^{K-1} \frac{e^T \tilde{\mathbf{A}}_s^T \mathbf{R}_s \tilde{\mathbf{A}}_s e}{e^T \mathbf{B}_s e} - \frac{1}{p\sigma^p ||e||^p} \sum_{i=0}^{r-1} (e_i - e_{i+1})^p \right\} \tag{3.14}$$

[1]Note that this expression is an improper probability density because it has an infinite integral. However, this technicality has no impact on the estimation.

We call the first term within the maximization the data term, $f_{STR}(e)$, and the second term the prior term $S_p(e, \sigma)$.

$$f_{STR}(e) = \frac{1}{2}\sum_{s=0}^{K-1}\frac{e^T\tilde{\mathbf{A}}_s^T\mathbf{R}_s\tilde{\mathbf{A}}_s e}{e^T\mathbf{B}_s e} \tag{3.15}$$

$$S_p(e,\sigma) = -\frac{1}{p\sigma^p||e||^p}\sum_{i=0}^{r-1}(e_i - e_{i+1})^p \tag{3.16}$$

3.2.3 Temporal regularization parameter determination

The temporal regularization parameter (σ) in Equation 3.14 is not known and therefore must be determined. This can be accomplished by minimizing the mean square (MS) error of the estimator ($||e-\hat{e}_\sigma||^2$) with respect to σ, where $\hat{e}_\sigma$ is the STR estimate. However, in real data, the true signal e is not known. Therefore, MS error cannot be determined.

Instead, we use crossvalidation (CV) methods [50, 51] to find the temporal regularization parameter. The "leave-one-out" CV strategy involves creating datasets with one voxel, y_n, removed from the original dataset $D^{(0)}$ to form a new synthetic dataset $D^{(n)}$. The estimator is applied to the new dataset, yielding the estimate $\hat{e}_\sigma^{(n)}$. The next step is to find the crossvalidation error between the forward model in Equation 3.1 applied to the estimate and voxel timecourse data.

$$\epsilon_\sigma^{(n)} = \min_{\beta_n}||y_n - \beta_n A_{s(n)}\hat{e}_\sigma^{(n)}||^2. \tag{3.17}$$

Note that β_n can be found using least squares estimation. The crossvalidation error is taken for each voxel and summed over the whole volume to achieve the total volume CV error

$$\epsilon_\sigma = \sum_{n=1}^{N}\epsilon_\sigma^{(n)}\ , \tag{3.18}$$

for the particular regularization parameter σ. The smoothing parameter that satisfies

$$\hat{\sigma} = \operatorname{argmin}_\sigma(\epsilon_\sigma) \tag{3.19}$$

is then chosen and $\hat{e}_{\hat{\sigma}}$ is the final estimate.

3.2.4 Comparison methods of data analysis

Two methods of data analysis were used to find estimates for comparison to our supertemporal resolution method. The first method was simple averaging (SA) of the mean and drift corrected voxel timecourses interpolated into the same time frame as the first slice. The interpolation is accomplished by multiplying the timecourses by the appropriate linear interpolation implemented using a matrix $\mathbf{H}_{s(n)}$ for each respective slice.

$$\text{(SA)} \qquad \hat{e}_\sigma = \frac{1}{N}\sum_{n=1}^{N} \mathbf{H}_{s(n)}\tilde{y}_n \tag{3.20}$$

The second method is based on a simple data model of additive Gaussian noise. The timecourses were shifted into the same time frame as the first slice similarly to the SA method.

$$\mathbf{H}_{s(n)}\tilde{y}_n = \alpha_n e + \omega_n \tag{3.21}$$

We use this data model and temporal regularization prior term introduced for STR in Equation 3.16 to form the MAP estimate for this data model. We call this method interpolation with regularization (IWR).

$$\text{(IWR)} \qquad \hat{e}_\sigma = \underset{e}{\text{argmax}} \left(\frac{1}{2} \frac{e^T (\sum_{s=1}^{K} \mathbf{H}_s \mathbf{R}_s \mathbf{H}_s^T) e}{e^T e} + S_p(e, \sigma) \right) \tag{3.22}$$

The crossvalidation method we introduced for STR is also used to find the regularization parameter in Equation 3.22.

3.3 Methods

3.3.1 Acquisition of human data

Whole-brain images of a healthy right-handed male subject were obtain using a 1.5 T GE Echospeed MRI Scanner. A 3 inch surface coil centered under the occipital prominence was used as the receive coil in order to improve signal-to-noise in the area around the visual cortex. T1-weighted anatomic images were acquired for reference using 2D axial spin echo with TE/TR = minimum full/500 ms, flip angle = 90^o,

Table 3.2
Parameters for the human datasets. Dataset 1 was taken for cluster extraction. In Datasets 2 and 3, the scans are repeated 3 times

Dataset	# of scans	TR (s)	# of cycles
1	1	2.0	4.5
2	3	2.0	3.5
3	3	0.5	3.5

matrix = 256x128, at 4 locations through the primary visual cortex with thickness of 3.5 mm, gap of 0.7 mm, and field-of-view 24 cm x 24 cm.

Seven functional BOLD weighted scans were then run at the same locations using 2D axial gradient echo echoplanar imaging with the common parameters of TE = 50ms, flip angle = 90^o, matrix = 64x64, and field-of-view = 24x24 cm. The other parameters are given in Table 3.2.

An experimental paradigm was played during the functional scans to induce neuronal stimulation. An 8 Hz flashing checkerboard (6 x 8 squares) was used as the activation state to stimulate visual cortex using the STIM software package (Neuroscan Inc., El Paso, Tx). The control state was a black screen. A randomly alternating fixation point was used throughout the paradigm to limit eye movement and set attention. The timing of the paradigm was 8 second lead-in, 4.5 cycles of 32 second control state followed by 32 second activation state, and an 8 second lead-out. In the scans using only 3.5 cycles, the same paradigm was used but the acquisition was stopped at the appropriate time. The paradigm was delivered through MRI-compatible fiber-optic googles (Avotec Inc., Stuart, FL).

3.3.2 Processing of human data

We used the Student's t statistic [29] as a method to select activated voxels in Dataset 1 (see Table 3.2). A threshold of 6.5 was chosen to ensure that the activated voxels were as spatially contiguous within the slices as possible while still obtaining a large number of voxels. Only the voxels above this threshold were used in the subsequent analyses.

We used clustered components analysis (CCA) [49] on the activated voxels in Dataset 1 and chose the cluster containing the most voxels. The penalty term in the CCA was multiplied by a factor of 2 to be more conservative in the clustering. Only the voxels contained in this cluster were considered for Datasets 2 and 3. In order to reduce computation time in subsequent analysis, only samples 21 to 60 (corresponding to slightly longer than one cycle). were used in Dataset 2 and samples 81 to 240 in Dataset 3 (see Table 3.2).

The conjugate gradient method was used to perform the numerical optimization in Equation 3.14 on the clustered voxels in Dataset 2. The Fletcher-Reeves method for estimating the Hessian matrix was used [58]. The linesearch algorithm was conducted using the secant method. If the secant method failed, a binary bracketing linesearch was used as a backup method.

The gradient of the data term in Equation 3.15 is

$$\nabla_e f(e) = \sum_{s=0}^{K-1} \frac{e^T \mathbf{B}_s e e^T \mathbf{\Gamma}_s - e^T \mathbf{\Gamma}_s e e^T \mathbf{B}_s}{(e^T \mathbf{B} e)^2} \ , \tag{3.23}$$

where

$$\mathbf{\Gamma}_s = \tilde{\mathbf{A}}_s^T \mathbf{R}_s \tilde{\mathbf{A}}_s \ . \tag{3.24}$$

Note that $\mathbf{B}_s$ and $\mathbf{\Gamma}_s$ for each slice are precomputed before the conjugate gradient algorithm for a large computational savings.

The gradient of the prior term $S_p(e, \sigma)$ contains the partial derivative vector quantities

$$\frac{\partial S_p(e,\sigma)}{\partial e_i} = -\frac{1}{\sigma^p ||e||^p} F_p(e) \ , \tag{3.25}$$

where

$$F_p(e) = \begin{cases} (e_i - e_{i+1})^{p-1} - \frac{e_i}{||e||^2} \sum_{i=0}^{r-1} (e_i - e_{i+1})^p & \text{if } i = 1 \\ (e_i - e_{i+1})^{p-1} - (e_{i-1} - e_i)^{p-1} - \frac{e_i}{||e||^2} \sum_{i=0}^{r-1} (e_i - e_{i+1})^p & \text{if } 1 < i < r-1 \\ -(e_{i-1} - e_i)^{p-1} - \frac{e_i}{||e||^2} \sum_{i=0}^{r-2} (e_i - e_{i+1})^p & \text{if } i = r-1 \end{cases} \tag{3.26}$$

We used $p = 2$ in our studies. Therefore, the gradient can be simplified and represented in matrix form as

$$\nabla_e S_2(e, \sigma) = -\frac{1}{\sigma^2 ||e||^2} \left(2e - e_- - e_+ - \frac{||e - e_+||^2 e}{||e||^2} \right) , \tag{3.27}$$

where e_+ and e_- are shifted versions of e and are defined as $(e_1, e_2, \cdots, e_{r-1}, e_{r-1})^T$ and $(e_0, e_0, e_1, \cdots, e_{r-1})^T$ respectively. The conjugate gradient method was initialized with the stimulus function (one when stimulated, zero when at rest). At each conjugate gradient step, the direction of the linesearch is constrained to have zero mean and zero drift. The resulting estimate is renormalized at each step to avoid overflow/underflow problems. Note that the renormalization does not affect the cost function in Equation 3.14.

The crossvalidation technique in Equation 3.19 requires optimization and is implemented in an iterative fashion using a standard golden section search technique [58] over the logarithm base 10 of the temporal regularization parameter σ. The golden section search was bracketed between $\sigma = 3.1623 \times 10^{-6}$ and 1×10^{-3} and allowed to run for 6 iterations.

The simple averaging estimator in Equation 3.20 is a closed form solution and was directly applied to Dataset 3. We use the same conjugate gradient framework as discussed above for optimization in the interpolation with regularization method on Dataset 3. The gradient of the IWR estimate data term (see Equation 3.22) is derived.

$$\nabla_e f_{IWR}(e) = \frac{||e||^2 (\sum_{s=0}^{K-1} \mathbf{H}_s \mathbf{R}_s \mathbf{H}_s^T) e - e^T (\sum_{s=1}^{K-1} \mathbf{H}_s \mathbf{R}_s \mathbf{H}_s^T) e e}{||e||^4} \tag{3.28}$$

The crossvalidation method introduced for STR was also used to find the temporal regularization parameter in this case.

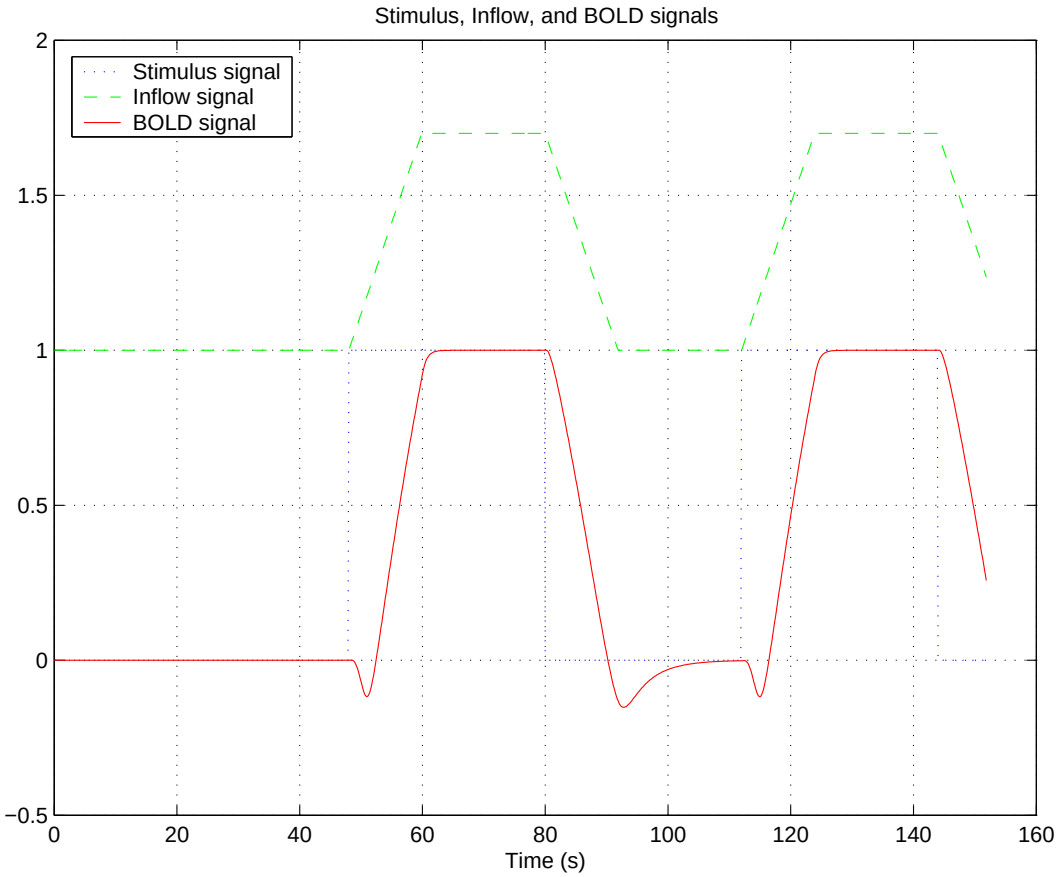

Fig. 3.2. Synthetic stimulus, inflow, and BOLD signals. This figure shows the the timing relationships between the synthetic signals. The BOLD signal was generated using the balloon model and was normalized with respect to the maximum amplitude.

3.3.3 Generation and processing of simulated data

We defined a 2.5 cycle stimulus signal with 64 seconds per cycle (32 seconds control, 32 seconds active) with lead-in of 16 seconds and lead-out of 8 seconds at a sampling period of 0.125 seconds (see Figure 3.2). A corresponding normalized inflow signal, $f_{in}(t)$, was generated from the stimulus signal with a peak of 1.7 and a 12 second rise/fall time following onset/resolution of the stimulus active state. See Figure 3.2 for the relationship between the stimulus and inflow signals.

The balloon model [8] was used to generate the BOLD signal, $S_{BOLD}(t)$, from the inflow signal, $f_{in}(t)$. The BOLD signal is explicitly derived in Appendix B.2. Refer to Figure 3.2 for the resulting BOLD response signal.

The goal of our techniques is to estimate the BOLD signal. However, the signal measured, even if no noise is present, is not the pure BOLD signal. The measured signal contains both BOLD and inflow effects. Therefore, we generated activation signals ΔS, which contained both inflow and BOLD signals, using Equation 3.29 [52]. Note that we are defining the activation signal as the change in total MR intensity signal, S, due to perturbations in hemodynamics arising from neuronal activation. The quantity $R_1^* = 1/T_1^*$ is the apparent longitudinal relaxation rate and $R_2^* = 1/T_2^*$ is the apparent transverse relaxation rate. Small changes in these values lead to changes in the activation signal and can be expressed using partial derivatives and the chain rule.

$$\Delta S(t) \;=\; \frac{\partial S}{\partial R_1^*}\Delta R_1^*(t) + \frac{\partial S}{\partial R_2^*}\Delta R_2^*(t) \tag{3.29}$$

The partial derivatives in Equation 3.29 ($\partial S/\partial R_1^*$ and $\partial S/\partial R_2^*$) can be derived from Equation 1 in reference [52]. These expressions are given by

$$\frac{\partial S}{\partial R_1^*} \;=\; M_0\, TR \frac{\sin(\alpha_{flip}) e^{-TE\, R_2^*} e^{-TR\, R_1^*} (1 - \cos(\alpha_{flip}))}{(1 - \cos(\alpha_{flip}) e^{-TR\, R_1^*})^2}\ , \tag{3.30}$$

$$\frac{\partial S}{\partial R_2^*} \;=\; -M_0\, TE \frac{\sin(\alpha_{flip}) e^{-TE\, R_2^*} (1 - e^{-TR\, R_1^*})}{1 - \cos(\alpha_{flip}) e^{-TR\, R_1^*}}\ . \tag{3.31}$$

The constants used in Equations 3.30 and Equation 3.31 are given in Table 3.3.

The temporal changes in the relaxation rates ($\Delta R_1^*(t)$ and $\Delta R_2^*(t)$) are related to normalized inflow changes ($\Delta f_{in}(t)$) and the normalized BOLD signal ($S_{BOLD}(t)$) through Equations 3.32 and 3.33. The maximum changes in the relaxation rates ($\Delta R_{1\,\max}^*$ and $\Delta R_{2\,\max}^*$) are given in Table 3.3.

$$\Delta R_1^*(t) \;=\; \Delta R_{1\,\max}^* \frac{\Delta f_{in}(t)}{\Delta f_{in\,\max}} \tag{3.32}$$

$$\Delta R_2^*(t) \;=\; \Delta R_{2\,\max}^* \frac{S_{BOLD}(t)}{S_{BOLD\,\max}}\ , \tag{3.33}$$

Table 3.3
Constants used for signal weighting in the data simulator. Note that these are typical values given in [52].

Constant	Value	Description
M_0	1	Normalized magnetization
α_{flip}	90^o	Flip angle
TE	40 ms	Time-to-echo
TR	0.5 s or 2.0 s	Time-to-repetition
R_1^*	1/(0.7 s)	Apparent longitudinal relaxation rate
R_2^*	1/(48 ms)	Apparent transverse relaxation rate
$\Delta R_{1\,\max}^*$	1.0 / min	Max change in long. relaxation rate
$\Delta R_{2\,\max}^*$	-0.5 / s	Max change in trans. relaxation rate

where $S_{BOLD\,\max}$ denotes the peak value of the BOLD signal and $\Delta f_{in\,\max}$ denotes the peak value of the change in normalized inflow. We used the values in Table 3.3 to generate the activation signals for TR = 2.0 s ($\Delta S_{2.0}$) and TR = 0.5 s ($\Delta S_{0.5}$) found in Figure 3.3.

We based our TR = 2.0 s synthetic datasets from a scan chosen from Dataset 2. First, the STR estimate $\hat{e}_{STR}$ was found from the chosen scan. Baseline (μ_n), drift (d_n), and activation amplitude (α_n), for each activated voxel timecourse (y_n) was found by taking a least squares fit of a vector of ones ($\vec{1}_m$), a zero-mean linear vector with slope of one (D_m), and the zero-mean, zero-drift normalized STR estimate ($\hat{e}_{STR}$), respectively. The subscript m denotes the number of timepoints. The standard deviation of the noise $\tilde{\sigma}_n$ was defined as the standard deviation of the residuals of the fit.

The parameters were then used to generate the synthetic datasets. The activation signal was subsampled to the appropriate TR with appropriate timeshifts to simulate the 2D acquisition using the matrices $\mathbf{G}_{s(n)}$ (see Table 3.1 for an example of slice

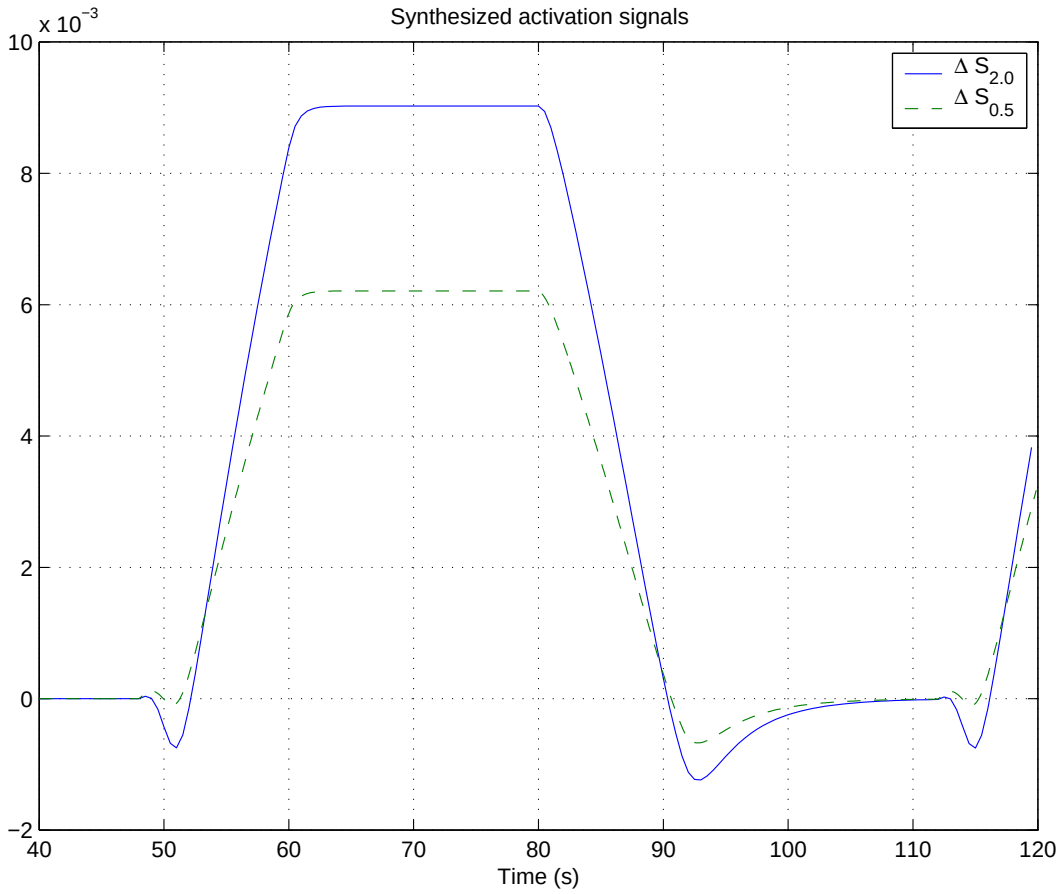

Fig. 3.3. Synthesized activation signals $\Delta S_{2.0}$ and $\Delta S_{0.5}$. Note the significant difference in the "initial dip" region. These signals (after normalization, baseline removal, and drift removal), were used to generate Datasets 4 and 5 (see Table 3.4) respectively. Although more timepoints were generated, only the timepoints between 40 and 120 seconds are shown for clarity.

Table 3.4
Summary of synthetic datasets The synthetic datasets were generated using $\kappa = 1, 2, 4, 6, 8$ for a total of 100 scans per dataset. Dataset 4 was generated using real Dataset 2 (see Table 3.2) parameters and Dataset 5 was generated using real Dataset 3 parameters.

Dataset	# of scans	TR (s)
4	20 / κ	2.0
5	20 / κ	0.5

timing using TR of 2 seconds and 4 slices). In order to simulate higher activation contrast when moving to higher field strengths, an amplitude amplification factor κ was introduced into the synthetic datasets at $\kappa = 1, 2, 4, 6, 8$. Each voxel timecourse in a synthetic dataset was generated using

$$y_n = \kappa\alpha_n \mathbf{G}_{s(n)} e_{TR} + \mu_n \vec{1}_m + d_n \vec{D}_m + \tilde{\sigma}_n N(0,1)_m \ , \tag{3.34}$$

where $N(0,1)_m$ is a randomly generated Gaussian independent, identically distributed vector, and $e_{TR} = \mathbf{P}[\Delta S(t)/\Delta S_{\max}]$ is the normalized, mean and drift removed activation signal. Note that $\mathbf{P}$ is the projection matrix defined in Equation 3.4.

The TR = 0.5 synthetic datasets were similarly generated from parameters extracted from a scan chosen from Dataset 3 with the IWR estimate $\hat{e}_{IWR}$. A summary of the synthetic datasets are found in Table 3.4. A diagram of the data simulator is given in Figure 3.4.

The simulated datasets were processed in the same manner as the human data. To reduce computation time, only the timepoints between 40 seconds and 120 seconds (samples 81 to 240 in Dataset 4 and samples 321 to 960 in Dataset 5) were considered. In order to investigate the performance of the crossvalidation strategy for finding regularization parameter, Dataset 4 was also analyzed using a minimum mean square error strategy instead of the minimum crossvalidation error method described above. This entailed using the golden section search over the logarithm base

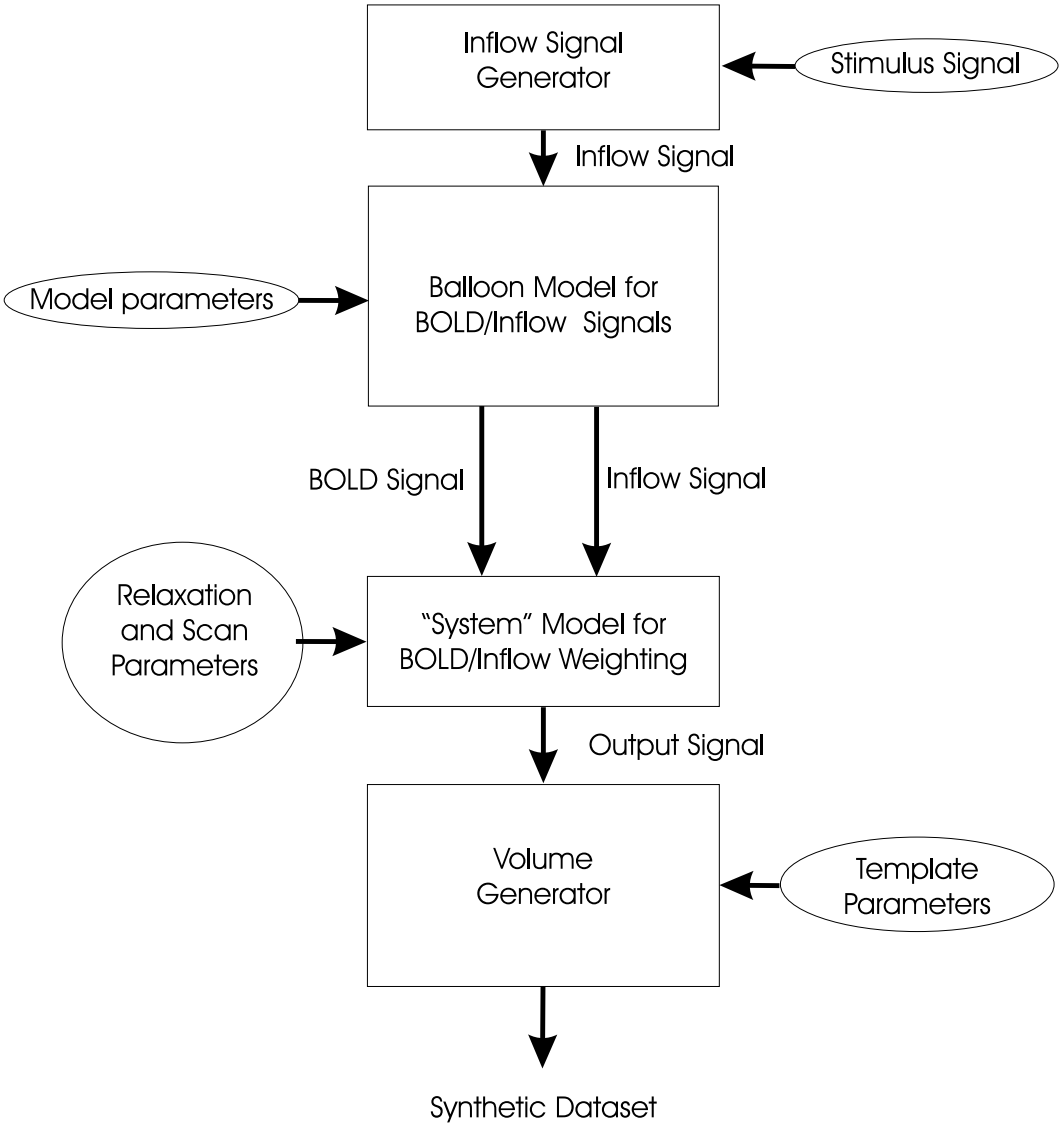

Fig. 3.4. Flow diagram of simulator used to generate simulated data. Examples of stimulus signal, inflow signal, and BOLD signal from the first 2 flow blocks are given in Figure 3.2. The balloon model parameters are given in Table B.1. Example output signals are given in Figure 3.3.

10 of the regularization parameter to minimize the mean square difference between appropriately fitted estimate and activation signal.

3.4 Results

3.4.1 Crossvalidation evaluation

The crossvalidation strategy was evaluated using the synthetic data using only the STR algorithm. First, STR estimates were found by determining the regularization parameter using the minimum crossvalidation (CV) error method. The mean square (MS) error of between these estimates ($\hat{e}_{STR}^{CV}$) and the normalized synthetic activation signal $e_{2.0}$ were calculated (the estimates were first least squares fitted to the synthetic activation signal). The STR estimates were then found by using a golden section search on the regularization parameter to find the minimum MS error. Figure 3.5 (a) shows an example of the minimization curves for the estimates in Figure 3.5 (b), which provides an example of the differences between estimates. The regularization parameters for the minimum MS and minimum CV error methods are displayed for the various amplitudes in Figure 3.6(a). The mean square difference between the minimum crossvalidation estimates and the minimum MS error estimates of each dataset. These differences were then normalized by the MS error of the minimum MS error estimate to produce a percent difference.

$$\%\text{diff} = \frac{(\hat{e}_{STR}^{CV} - \hat{e}_{STR}^{MS})^T(\hat{e}_{STR}^{CV} - \hat{e}_{STR}^{MS})}{(\hat{e}_{STR}^{MS} - e_{2.0})^T(\hat{e}_{STR}^{MS} - e_{2.0})} \times 100 \tag{3.35}$$

The results are plotted in for the various amplitudes in Figure 3.6 (b).

3.4.2 Comparative perfomance

The SA, IWR, and STR estimators were applied to the appropriate datasets, and the MS error was found between the estimates and the injected BOLD signal. The MS errors between injected activation signals and the BOLD signals were also found for reference. The results were plotted in Figure 3.7. Examples of the IWR and STR

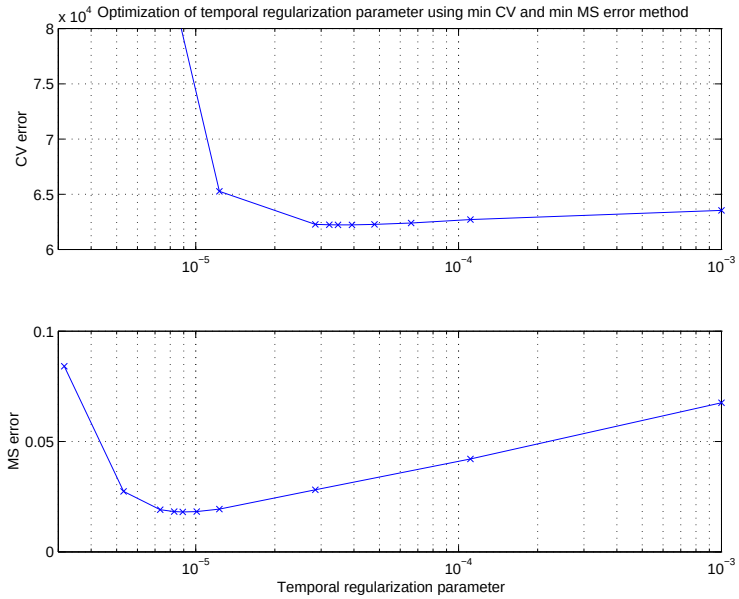

(a)

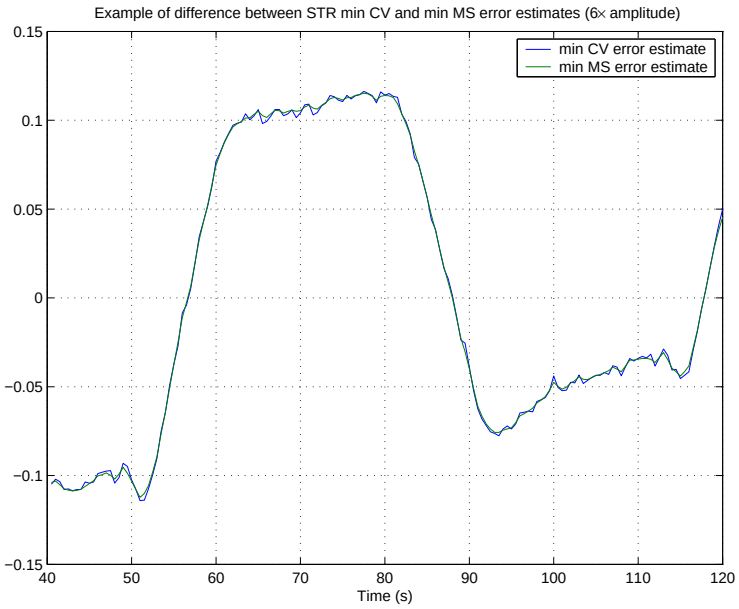

(b)

Fig. 3.5. Example of the difference between minimum crossvalidation (CV) and minimum mean square (MS) error estimates on the same dataset (at 6x amplitude): (a) Minimization traces of CV (upper plot) error and MS (lower plot) error versus regularization parameter. (b) Actual estimates, Note that the estimates in (b) are qualitatively almost identical even though the regularization parameters at the minima in (a) are quite different.

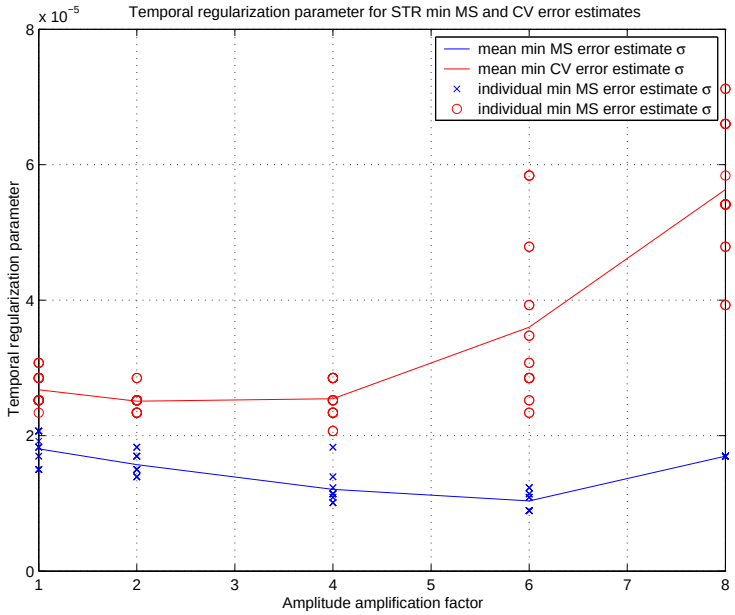

(a)

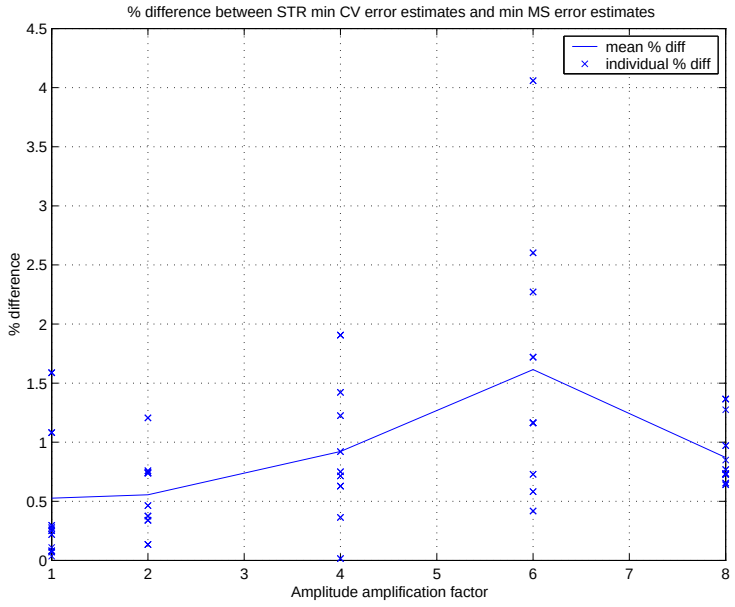

(b)

Fig. 3.6. Characteristics of the minimum crossvalidation error method for the various amplitudes: (a) regularization parameters found using the minimum CV and minimum MS error methods, (b) percent difference using Equation 3.35. The solid lines represent mean values and individual points represent individual estimates. Note that even though the mean values of the regularization parameters in (a) are quite different, the mean percent difference in (b) remains below 2%.

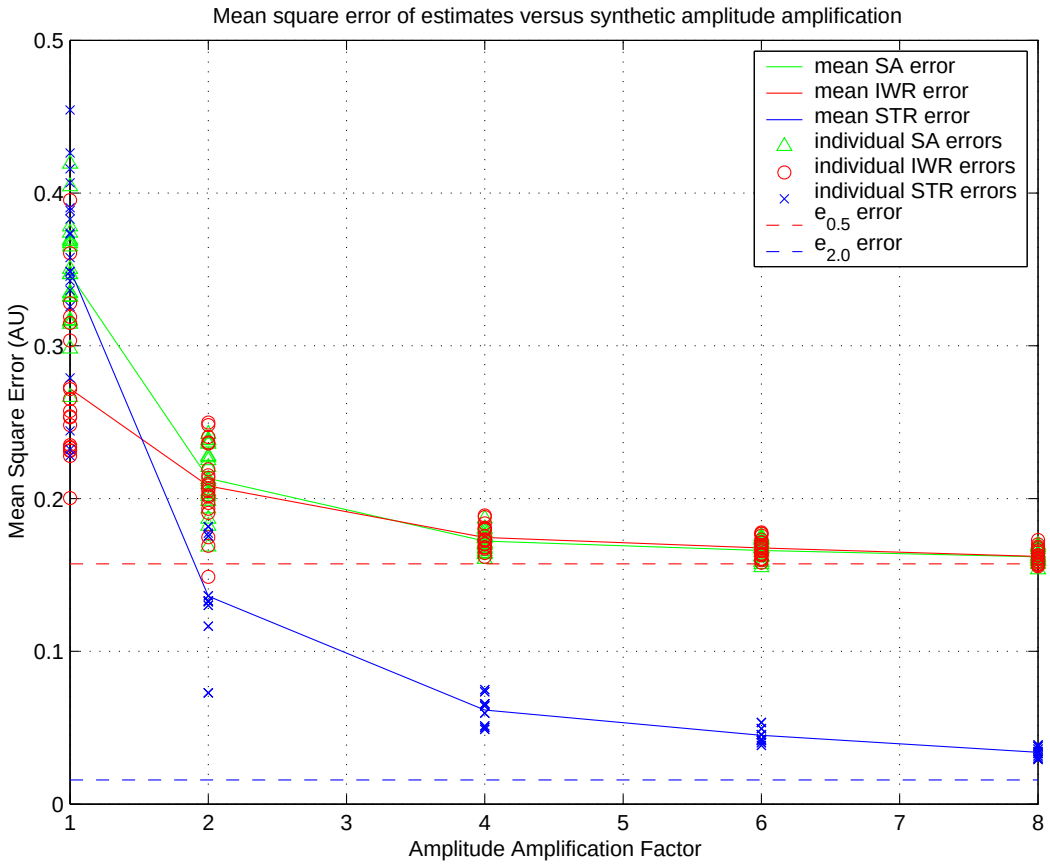

Fig. 3.7. Estimator error results for varying the activation amplitude in the synthetic data (blue = supertemporal resolution (STR), red = interpolation with regularization (IWR), and green = simple averaging (SA)). The dashed lines represent the the baseline errors between the activation signals and the BOLD signal. Essentially, they are the lower bound of the performace of each analysis method. The solid lines represent the mean error at each timepoint for each analysis method. The individual points represent the error for each estimate. Note that although the mean error for the STR estimates at 1x amplitude is greater than that of the IWR estimates, it quickly falls lower than IWR for 2x and higher.

estimates at 4× activation amplitude are presented in Figure 3.8.

3.4.3 Human data

Two hundred and two total activated voxels were found in the Student's t thresholding of Dataset 1 (see Table 3.2). The largest cluster of 99 voxel locations was chosen after application of the CCA method.

The simple averaging estimates using Dataset 3 are shown in Figure 3.9(a), along with a mean and standard deviation plot (Figure 3.9(b)). The interpolation with regularization estimates using Dataset 3 are shown in Figure 3.9(c), along with a mean and standard deviation plot (Figure 3.9(d)). The supertemporal resolution estimates using Dataset 4 are shown in Figure 3.9(e), along with a mean and standard deviation plot (Figure 3.9(f)). Note that the estimates in Figure 3.9(a), (c), and (d) are fitted to an arbitrary estimate in the set.

3.5 Discussion and Conclusion

3.5.1 Crossvalidation evaluation

It can be seen in Figure 3.6(a) and Figure 3.5(b) that the minimum crossvalidation error technique does not yield the same temporal regularization parameter as the minimum MS error. It would be quite fortunate if the regularization parameters from minimum CV and mininimum MS error were similar. However, the primary aim of our technique is NOT to find temporal smoothness, but to find a good estimate of the response signal. Figure 3.5(a), shows that the temporal regularization found by using the minimum CV error method (in the top graph) still produces a MS error (lower graph). Therefore, the metric we use to determine "goodness" was given in Equation 3.35, which is a ratio of the closeness of the minimum CV and minimum MS error estimates to the mean square error of the mininum MS error estimate. Figure 3.6(b) shows that the metric stays under 5% for all the simulations, and under 2%

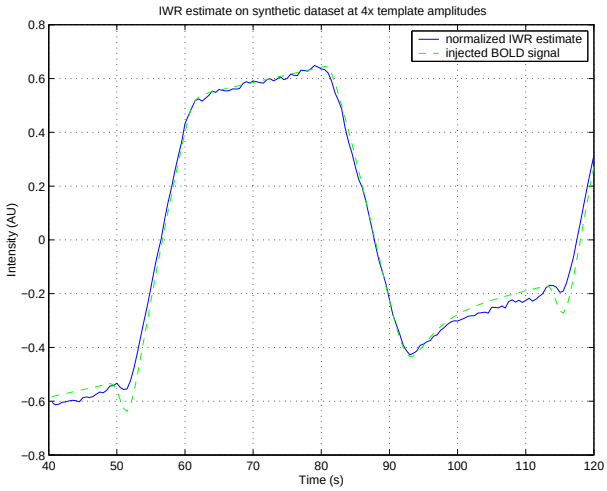

(a)

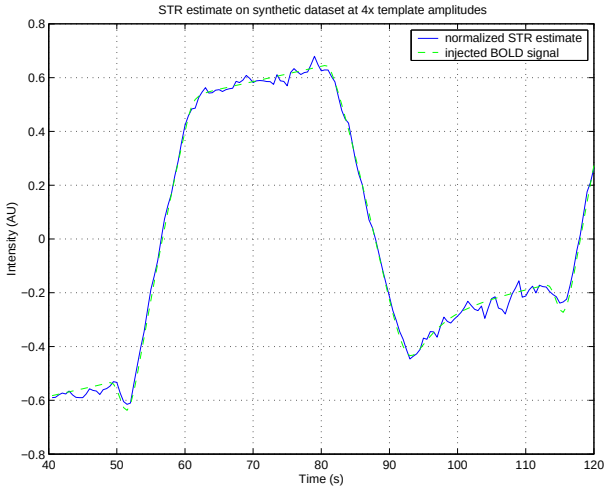

(b)

Fig. 3.8. Examples of interpolation with regularization (IWR) and supertemporal resolution (STR) estimates at 4x amplitude in synthetic data: (a) IWR estimate, (b) STR estimate. The solid lines represent the fitted estimates and the dashed lines represent the BOLD signal. Notice that the STR estimate in (b) more closely follows the BOLD signal than the IWR estimate in (a), especially in the region of the "initial dip."

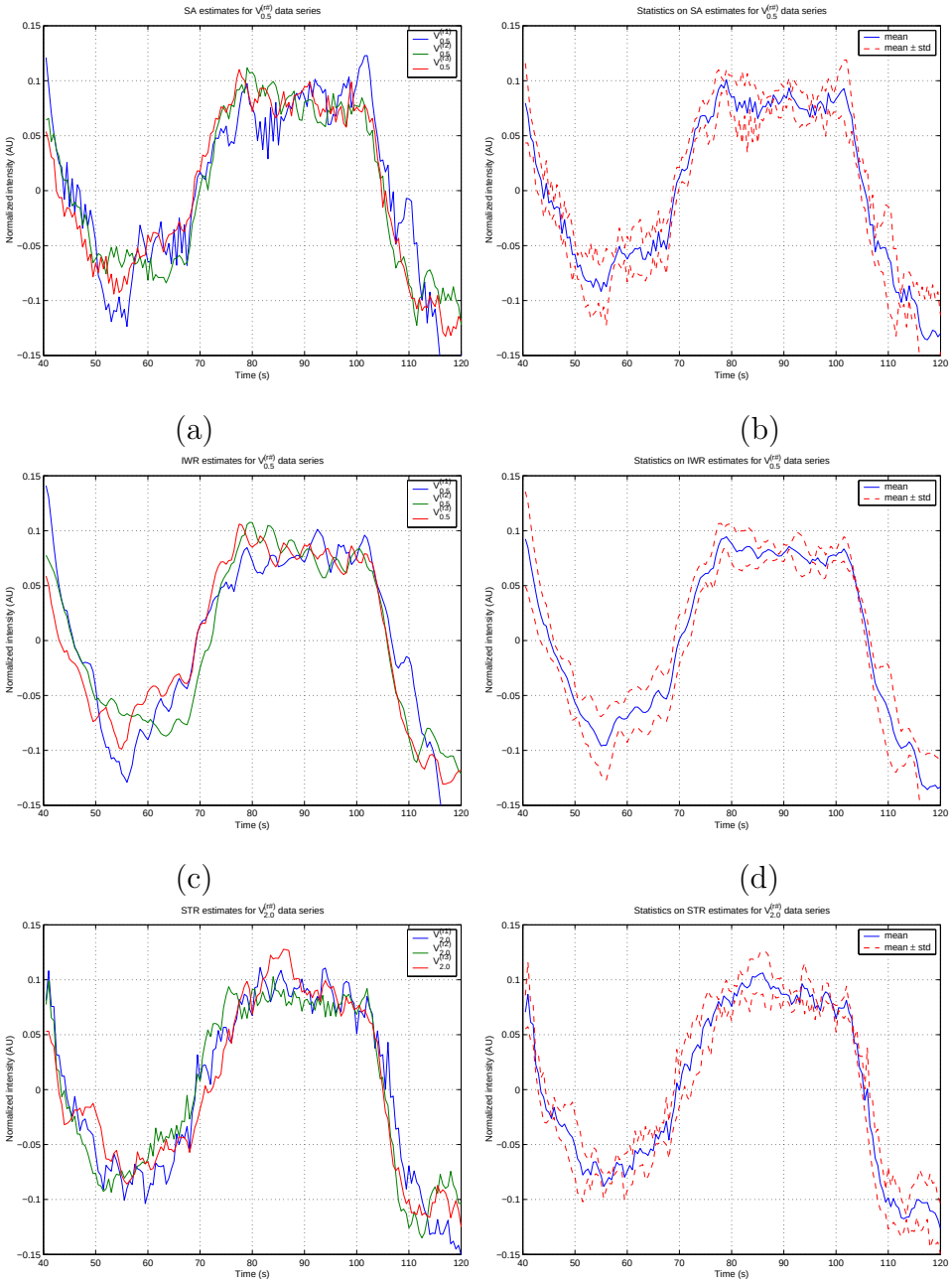

Fig. 3.9. Results for the analysis of human data: (a) simple averaging (SA) estimates on Dataset 2 (see Table 3.2), (b) mean and standard deviation of the SA estimates on Dataset 2, (c) interpolation with regularization (IWR) estimates on Dataset 2, (d) mean and standard deviation of the IWR estimates on Dataset 2, (e) supertemporal resolution (STR) estimates on Dataset 3, (f) mean and standard deviation of STR estimates on Dataset 3.

for all but a few. Figure 3.5(b) shows qualitatively the similarities between the two estimates, and is typical of all the datasets. We conclude that the minimum crossvalidation error technique is an effective method for temporal regularization parameter determination.

3.5.2 Estimator performance

Figure 3.7 shows the performance of the SA, IWR, and STR estimators as the simulated activation amplitude is increased. The dashed lines represent the mean square error between injected signal and the BOLD signal. The difference between them reflects the physical advantage of reduction in inflow effects when using a longer TR. These serve as a baseline measurement for comparison of the estimators.

It can be seen at the initial activation amplitude that the IWR estimator performs better than both SA and STR estimators. We speculate that this is due to the IWR estimator incorporating both more data and temporal regularization. However, as the activation amplitudes progressively get larger (such as in the case of increasing static field strengths), the SA and IWR converge to to similar error statistics while the physical advantage of the STR method becomes clearly evident.

The examples of the IWR and STR estimates at 4x activation amplitude in Figure 3.8 clearly show the differences. In Figure 3.8(a), it is seen for the IWR estimate that the "initial dip" has been severely distorted and the "post stimulus undershoot" has also been decreased. The STR estimate retains these characteristics, albeit with slightly more noise.

3.5.3 Human data results

In Figure 3.9(a) and (b), the SA estimates are qualitatively more noisy than in Figure 3.9(c) and (d) because the IWR utilized temporal regularization. Note that the mean results have qualitatively the same shape because both methods are applied to Dataset 2. Figure 3.9(e) and (f) show the results for STR estimates. These estimates

are qualitatively noisier than the IWR estimates because Dataset 3 contains a quarter of the timepoints of Dataset 2. Although the STR results are qualitatively different than the IWR/SA results, no clear-cut conclusions are drawn on the mechanisms behind the differences.

3.5.4 Conclusions

In this chapter, we have introduced a unique technique for the analysis of fMRI timeseries data. The supertemporal resolution method allows the user to obtain a high resolution estimate without introducing confounding blood inflow effects that accompany acquisition at short TR. This method utilizes a novel Bayesian prior model to implement temporal regularization and a crossvalidation strategy for determining the amount of regularization.

We also introduced a new data simulator to test analysis techniques. It incorporates parameters estimated from real human experiments and generates signals based upon the balloon model. The simulator utilizes acquisition parameters to properly weight BOLD and blood inflow effects in the activation signal.

The techniques introduced in this chapter will allow investigators to study the temporal evolution of the BOLD response and help to further elucidate the underlying mechanisms.

4. RECOMMENDATIONS

In this thesis, I have presented a framework for the analysis of functional MRI time-series data. During the course of the development of the methods, I pondered many additions and improvements that could be made to the framework. Many experiments were also considered but never carried out. Although these ideas were never implemented, I will suggest them in this chapter.

4.1 Algorithmic improvements

4.1.1 Approximation in the crossvalidation method

Running the crossvalidation strategy discussed in Chapter 3 on each synthetic dataset for a number of regularization parameters can be quite computationally expensive. We can use a multivariate Taylor's approximation to find a closed form solution for each $e_\sigma^{(n)}$ given an initial point $e_\sigma^{(0)}$ near the solution. This initial point can be the estimate for the full dataset $D^{(0)}$ and will be near the solution because subtracting one pixel to form the synthetic datasets will perturb the cost function in Equation 3.14 only slightly. We denote the cost function of the synthetic dataset $D^{(n)}$ as $Q_\sigma^{(n)}$ and the Hessian as $\mathbf{H}_\sigma^{(n)}$ for a given regularization parameter σ. The Taylor's approximation can then be written in terms of the gradient of the cost function.

$$e_\sigma^{(n)} = e^{(0)} - \mathbf{H}_\sigma^{(n)\,-1}(e^{(0)})\nabla_e Q_\sigma^{(n)}(e^{(0)}) \; . \tag{4.1}$$

This will reduce the computational complexity by an enormous amount due to the fact that iterations of a linesearch need not be performed. However, the Hessian of

the cost function $\mathbf{H}$ must be found. For the data term, the Hessian of the full dataset is given by

$$\mathbf{H}_f^{(0)}(e) = \sum_{i=0}^{K-1} \frac{1}{\kappa_i^2} \left(\kappa_i \mathbf{G}_i - \gamma_i \mathbf{B}_i - 2\mathbf{B}_i e e^t \mathbf{G}_i - 2\mathbf{G}_i e e^t \mathbf{B}_i + 4\frac{\gamma_i}{\kappa_i} \mathbf{B}_i e e^t \mathbf{B}_i \right) . \quad (4.2)$$

The Hessian of the prior term for $p = 2$ is then

$$\begin{aligned} &\mathbf{H}_S(e) = \\ &-\frac{1}{\sigma^2 ||e||^2} \left(2\mathbf{I}_N - \mathbf{S}_N - \frac{2}{||e||^2} (e(2e - e_- - e_+)^t + (2e - e_- - e_+)e^t) \right. \\ &\left. -\frac{||e - e_-||^2}{||e||^2} \quad (\mathbf{I}_N + \frac{4}{||e||^2} e e^t) \right) \end{aligned} \quad (4.3)$$

where $\mathbf{S}_N$ is a symmetric matrix with ones on the subdiagonal and superdiagonal and zeros elsewhere. The Hessian for the cost function of the full dataset is then $\mathbf{H}^{(0)}(e) = \mathbf{H}_f^{(0)}(e) + \mathbf{H}_S(e)$. In order to find the Hessian of the reduced dataset $D^{(i)}$, all that is necessary is to subtract the Hessian of the data term of the deleted pixel $\mathbf{h}^{(i)}(e)$ from the full Hessian $\mathbf{H}^{(0)}(e)$. Verification that this linear approximation technique yields a solution for estimate that is close to that of MS error and full crossvalidation error analysis is needed.

4.1.2 Combination of CCA and STR

At this point in time, we use CCA as a preprocessing step to fulfill the assumption in the STR method that all voxel timecourses considered have the same behavior. A more elegant modification of the framework would be to combine both CCA and STR analysis into one unified algorithm. I have derived some equations to this end, but have not yet implemented them.

The voxelwise likelihood function can be expressed as a hybrid between the log likelihood in Equation 2.20 in Chapter 2 and the likelihood in Equation 3.8 in Chapter 3. Note that the equation includes the observation matrix $A_{s(n)}$ from the STR method at the set of component vectors E_K from the CCA method.

$$p_{y_n|x_n}(y_n|k, E_K, \hat{\alpha}_n) = \frac{1}{(2\pi)^{\frac{M-1}{2}}} \exp\left\{ -\frac{1}{2} \left[y_n^t y_n - \frac{(y_n^t A_{s(n)} e_k)^2}{e_k^t A_{s(n)}^t A_{s(n)} e_k} \right] \right\} \quad (4.4)$$

The posterior probabilities are formed from the likelihood function in Equation 4.4 and the prior probabilities that are defined in Chapter 2 (similar to Equation 2.28).

$$p_{x_n|y_n}(k|y_n, E_K, \Pi_K, \hat{\alpha}_n) = \frac{p_{y_n|x_n}(y_n|k, E_K, \hat{\alpha}_n)\pi_k}{\sum_{l=1}^{K} p_{y_n|x_n}(y_n|l, E_K, \hat{\alpha}_n)\pi_l} \tag{4.5}$$

The total log-likelihood is expressed in the same way as Equation 2.26 in Chapter 2.

$$\log p_y(y|K, E_K, \Pi_K, \hat{\alpha}) = \sum_{n=1}^{N} \log \left(\sum_{k=1}^{K} p_{y_n|x_n}(y_n|k, E_K, \hat{\alpha}_n)\pi_k \right) \tag{4.6}$$

The expectation step of the EM algorithm is then expressed as the following two equations.

$$\bar{N}_{k|K} = \sum_{n=1}^{N} p_{x_n|y_n}(k|y_n, E_K^{(i)}, \Pi_K^{(i)}, \hat{\alpha}_n) \tag{4.7}$$

$$\bar{R}_{k|K,s} = \sum_{n \in \text{slice}\{s\}} \left\{ y_n y_n^t p_{x_n|y_n}(k|y_n, E_K^{(i)}, \Pi_K^{(i)}, \hat{\alpha}_n) \right\} \tag{4.8}$$

The maximization step of the EM algorithm can also be expressed.

$$\pi_k^{(i+1)} = \frac{\bar{N}_k}{N} \tag{4.9}$$

$$e_k^{(i+1)} = \underset{e_k}{\text{argmax}} \sum_{s=1}^{S} \frac{e_k^t A_s^t \bar{R}_{k|K,s} A_s e_k}{e_k^t A_s^t A_s e_k} \ , \tag{4.10}$$

where the latter equation can be solved using numerical methods.

The temporal regularization discussed in Chapter 3 may be implemented by adding the prior model in Equation 3.16 to the argument of the maximization in Equation 4.10 and substituting e_k for e. Implementation of the order identification (estimation of K) and crossvalidation requires further effort.

4.2 Human experiments

As said in Chapter 3, the STR human experiments run at 1.5 T had too low of an SNR to draw good physical and physiologic conclusions about the differences between the STR and the IWR estimates. It would be quite interesting to run the same human experiments at higher field strengths to increase SNR and see if difference do exist.

Because neither CCA nor STR have the constraint of periodicity, other experiments using event-related paradigms could be implemented and analyzed using our methods. In these cases, the faster moving features of the BOLD response are even more important, and the advantages of STR may be exploited further than using block paradigms. As we have only used visual stimuli in our experiments for STR, it would also be interesting to run experiments stimulating other cortices.

LIST OF REFERENCES

LIST OF REFERENCES

[1] S. Ogawa, T. M. Lee, A. R. Kay, and D. W. Tank. Brain magnetic resonance imaging with contrast dependent on blood oxygenation. *Proc. Natl. Acad. Sciences*, 87:9868–9872, 1990.

[2] K. K. Kwong, J. W. Belliveau, D. A. Chesler, I. E. Goldberg, R. M. Weisskoff, B. P. Poncelet, D. N. Kennedy, B. E. Hoppel, M. S. Cohen, R. Turner, H. Cheng, T. J. Brady, and B. R. Rosen. Dynamic magnetic resonance imaging of human brain activity during primary sensory stimulation. *Proc. Natl. Acad. Sciences*, 89:5675–5679, 1992.

[3] J. W. Belliveau, D. N. Kennedy, R. C. McKinstry, B. R. Buchbinder, R. M. Weisskoff, M. S. Cohen, J. M. Vevea, T. J. Brady, and B. R. Rosen. Functional mapping of the human visual cortex by magnetic resonance imaging. *Science*, 254:716–719, 1991.

[4] P. A. Bandettini, E. C. Wong, , R. S. Hinks, R. S. Tikofsky, and J. S. Hyde. Time course EPI of human brain function during task activation. *Magnetic Resonance in Medicine*, 25:390–397, 1992.

[5] P. A. Bandettini, A. Jesmanowicz, E. C. Wong, and J. S. Hyde. Processing strategies for time-course data sets in functional MRI of the human brain. *Magnetic Resonance in Medicine*, 30:161–173, 1993.

[6] K. J. Friston, P. Jezzard, and R. Turner. Analysis of functional MRI time-series. *Human Brain Mapping*, 2:69–78, 1994.

[7] G. M. Hathout, S. S. Gambhir, R. K. Gopi, K. A. Kirlew, Y. Choi, G. So, D. Gozal, R. Harper, R. B. Lufkin, and R. Hawkins. A quantitative physiologic model of blood oxygenation for functional magnetic resonance imaging. *Investigative Radiology*, 30(11):669–682, November 1995.

[8] R. B. Buxton, E. C. Wong, and L. R. Frank. Dynamics of blood flow and oxygenation changes during brain activation: the balloon model. *Magnetic Resonance in Medicine*, 39:855–864, 1998.

[9] F. Kruggel and D. Y. von Cramon. Temporal properties of the hemodynamic response in functional MRI. *Human Brain Mapping*, 8:259–271, 1999.

[10] V. Solo, P. Purdon, R. Weisskoff, and E. Brown. A signal estimation approach to functional MRI. *IEEE Trans. on Medical Imaging*, 20(1):26–35, January 2001.

[11] G. M. Boynton, S. A. Engel, G. H. Glover, and D. J. Heeger. Linear systems analysis of functional magnetic resonance imaging in human V1. *J. of Neuroscience*, 16(13):4207–4221, 1996.

[12] M. S. Cohen. Parameteric analysis of fMRI data using linear systems methods. *Neuroimage*, 6:93–103, 1997.

[13] J. J. Sychra, P. A. Bandettini, N. Bhattacharya, and Q. Lin. Synthetic images by subspace transforms I. Principal components images and related filters. *Medical Physics*, 21(2):193–201, February 1994.

[14] W. Backfrieder, R. Baumgartner, M. Samal, E. Moser, and H. Bergmann. Quatification of intensity variations in functional MR images using rotated principal components. *Physics in Medicine and Biology*, 41:1425–1438, 1996.

[15] M. J. McKeown, S. Makeig, G. G. Brown, T.-P. Jung, S. S. Kindermann, A. J. Bell, and T. J. Sejnowski. Analysis of fMRI data by blind separation into independent spatial components. *Human Brain Mapping*, 6:160–188, 1998.

[16] M. J. McKeown, T-P Jung, S. Makeig, G. Brown, S. S. Kindermann, T-W Lee, and T. J. Sejnowski. Spatially independent activity patterns in functional MRI data during the Stroop color-naming task. *Proc. Natl. Acad. Sciences*, 95:803–810, 1998.

[17] C. Goutte, P. Toft, E. Rostrup, F. A. Nielsen, and L. K Hansen. On clustering fMRI time series. *Neuroimage*, 9:298–310, 1999.

[18] K-H Chuang, M-J Chiu, C-C Lin, and J-H Chen. Model-free functional MRI analysis using kohonen clustering neural network and fuzzy c-means. *IEEE Trans. on Medical Imaging*, 18(12):1117–1128, December 1999.

[19] X. Golay, S. Kollias, G. Stoll, D. Meier, A. Valvanis, and P. Boesiger. A new correlation-based fuzzy logic clustering algorithm for fMRI. *Magnetic Resonance in Medicine*, 40:249–260, 1998.

[20] A. Baune, F. T. Sommer, M. Erb, D. Wildgruber, B. Kardatzki, Palm, and Grodd. Dynamical cluster analysis of cortical fMRI activation. *Neuroimage*, 9:477–489, 1999.

[21] E. T. Bullmore, S. Rabe-Hesketh, R. G. Morris, L. Gregory S. C. R. Williams, J. A. Gray, and M. J. Brammer. Function magnetic resonance image analysis of a large-scale neurocognitive network. *Neuroimage*, 4(1):16–33, August 1996.

[22] S. Chen, C. A. Bouman, and M. J. Lowe. Harmonic decomposition and eigenanalysis of BOLD fMRI timeseries data in different functional cortices. In *Proc. of the ISMRM Eighth Scientific Meeting*, page 817, Denver, April 3-7 2000.

[23] B.A. Ardekani, J. Kershaw, K. Kashikura, and I. Kanno. Activation detection in functional MRI using subspace modeling and maximum likelihood estimation. *IEEE Trans. on Medical Imaging*, 18(2):101–114, 1999.

[24] A. F. Sole, S.-C. Ngan, G. Sapiro, X. Hu, and A. Lopez. Anisotropic 2-D and 3-D averaging of fMRI signals. *IEEE Trans. on Medical Imaging*, 20(2):86–93, February 2001.

[25] A. P. Dempster, N. M. Laird, and D. B. Rubin. Maximum likelihood from incomplete data via the EM algorithm. *Journal of the Royal Statistical Society B*, 39(1):1–38, 1977.

[26] E. Redner and H. Walker. Mixture densities, maximum likelihood and the EM algorithm. *SIAM Review*, 26(2), April 1984.

[27] J. Rissanen. A universal prior for integers and estimation by minimum description length. *The Annals of Statistics*, 11(2):417–431, September 1983.

[28] C. A. Bouman. Cluster: an unsupervised algorithm for modeling Gaussian mixtures. Available from http://www.ece.purdue.edu/~bouman, April 1997.

[29] M. J. Lowe and D. P. Russell. Treatment of baseline drifts in fMRI time series analysis. *Journal of Computer Assisted Tomography*, 23(3):463–473, 1999.

[30] Z. Liang, R. J. Jaszczak, and R. E. Coleman. Parameter estimation of finite mixtures using the EM algorithm and information criteria with applications to medical image processing. *IEEE Trans. on Nuclear Science*, 39(4):1126–1133, 1992.

[31] M. J. Lowe, M. Dzemidzic, J. T. Lurito, V. P. Mathews, and M. D. Phillips. Functional discrimination of thalamic nuclei using BOLD contrast at 1.5T. In *Proc. of the Int'l Society of Mag. Res. in Med.*, page 888, Denver, April 1-7 2000.

[32] M. D. Phillips, M. J. Lowe, J. T. Lurito, M. Dzemidzic, and V. P. Matthews. Temporal lobe activation demonstrates sex-based differences during passive listening. *Radiology*, 220(1):202–207, July 2001.

[33] M. J. Lowe, J. T. Lurito, V. P. Matthews, M. D. Phillips, and G. D. Hutchins. Quantitative comparison of functional contrast from BOLD-weighted spin-echo and gradient-eco echoplanar imaging at 1.5T and H2 150 PET in the whole brain. *J. of Cerebral Blood Flow and Metabolism*, 20(9):1331–40, September 2000.

[34] P. Purdon, V. Solo, E. M. Brown, and R. Weisskoff. Functional MRI signal modeling with spatial and temporal correlations. *Neuroimage*, 14(4):912–923, Oct 2001.

[35] S. Makeig. EEG/ICA toolbox for Matlab. Available from http://www.sccn.ucsd.edu/~scott/ica.html, September 2001.

[36] A. L. Vazquez and D. C. Noll. Nonlinear aspects of the BOLD response in functional MRI. *Neuroimage*, 7:108–118, 1998.

[37] R. A. Johnson and D. W. Wichern. *Applied Multivariate Statistical Analysis,* 4^{th} *ed.* Prentice-Hall, Inc., Upper Saddle, NJ, 1998.

[38] K. J. Friston, C. D. Frith, P. F. Liddle, and R. S. Frackowiak. Functional connectivity: The principal-component analysis of large (PET) data sets. *J. of Cerebral Blood Flow and Metabolism*, 13(1):5–14, 1993.

[39] A. J. Bell and T. J. Sejnowski. An information maximization approach to blind separation and blind deconvolution. *Neural Computation*, 7:1129–1159, 1995.

[40] K. J. Friston. Modes or models: a critique on independent component analysis for fMRI. *Trends in cognitive sciences*, 2(10):373–375, October 1998.

[41] M. J. McKeown and T. J. Sejnowski. Independent component analysis of fMRI data: Examining the assumptions. *Human Brain Mapping*, 6:368–372, 1998.

[42] R. Baumgartner, C. Windischberger, and E. Moser. Quantification in functional magnetic resonance imaging: Fuzzy clustering vs. correlation analysis. *Magnetic Resonance Imaging*, 16(2):115–125, 1998.

[43] C. Goutte, L. K. Hansen, M. G. Liptrot, and E. Rostrup. Feature-space clustering for fMRI meta-analysis. *Human Brain Mapping*, 13:165–183, 2001.

[44] J. G. Brankov, N. P. Galatsanos, Y. Yang, and M. N. Wernick. Similarity based clustering using the expectation maximization algorithm. In *Proc. of IEEE Int'l Conf. on Image Proc.*, page *to appear*, Rochester, September 22-25 2002.

[45] J. Sijbers, A. J. den Dekker, J. Van Audekerke, M. Verhoye, and D. Van Dyck. Estimation of the noise in magnitude mr images. *Magnetic Resonance Imaging*, 16(1):87–90, 1998.

[46] R. B. Buxton. The elusive initial dip. *Neuroimage*, 13:953–958, 2001.

[47] I. Vanzetta and A. Grinvald. Evidence and lack of evidence for the initial dip in the anesthetized rat: Implications for human functional brain imaging. *Neuroimage*, 13:959–967, 2001.

[48] N. Nguyen, P. Milanfar, and G. Golub. A computationally efficient superresolution image reconstruction algorithm. *IEEE Trans. on Image Processing*, 10(4):573–583, April 2001.

[49] C. A. Bouman, S. Chen, and M. J. Lowe. Clustered component analysis for fMRI signal classification and estimation. In *Proc. of IEEE Int'l Conf. on Image Proc.*, volume 1, pages 609–612, Vancouver, Canada, September 10-13 2000.

[50] M. Stone. Cross-validatory choice and assessment of statistical predictions. *J. of the Royal Statistical B*, 2:111–147, 1974.

[51] G. Wahba and S. Wold. Periodic splines for spectral density estimation: The use of cross-validation for determining the degree of smoothing. *Communications in Statistics*, 4(2):125–141, 1975.

[52] G. H. Glover, S. K. Lemieux, M. Drangova, and J. M. Pauly. Decomposition of inflow and blood oxygen level-dependent (BOLD) effects with dual-echo spiral gradient-recalled (GRE) fMRI. *Magnetic Resonance in Medicine*, 35:299–308, 1996.

[53] S-G Kim, W. Richter, and K. Uğurbil. Limitations of temporal resolution in functional MRI. *Magnetic Resonance in Medicine*, 37:631–636, 1997.

[54] A. Tikhonov and V. Arsenin. *Solutions of Ill-Posed Problems*. Winston and Sons, New York, 1977.

[55] T. Hebert and R. Leahy. A generalized EM algorithm for 3-D Bayesian reconstruction from Poisson data using Gibbs priors. *IEEE Trans. on Medical Imaging*, 8(2):194–202, June 1989.

[56] D. Geman and G. Reynolds. Constrained restoration and the recovery of discontinuities. *IEEE Trans. on Pattern Analysis and Machine Intelligence*, 14(3):367–383, 1992.

[57] C. A. Bouman and K. Sauer. A generalized Gaussian image model for edge-preserving MAP estimation. *IEEE Trans. on Image Processing*, 2(3):296–310, July 1993.

[58] E. K. P. Chong and S. H. Żak. *An Introduction to Optimization*. John Wiley & Sons, Inc., New York, 1996.

APPENDICES

APPENDIX A
DERIVATIONS FOR CLUSTERED COMPONENTS ANALYSIS

A.1 Derivation of noise covariance

In this appendix, we derive an estimate for the noise covariance matrix of the noise subspace. Using equation (2.7), and defining the matrix $P_A = A(A^tA)^{-1}A^t$ results in the relation $\epsilon = (I - P_A)\nu$. Using the assumption that the noise is white, we have $I\sigma^2 = \frac{1}{N}E\left[\nu\nu^t\right]$ where I is an identity matrix and σ is the variance of the noise. From this we know that $\sigma^2 = \frac{1}{NP}E\left[tr\left\{\nu\nu^t\right\}\right]$. Using these results, we derive the following.

$$\begin{aligned} E\left[tr\left\{\epsilon\epsilon^t\right\}\right] &= \sigma^2 E\left[tr\left\{(I-P_A)\nu\nu^t(I-P_A)^t\right\}\right] \\ &= \sigma^2 tr\left\{(I-P_A)E\left[\nu\nu^t\right](I-P_A)^t\right\} \\ &= \sigma^2 N tr\left\{(I-P_A)(I-P_A)^t\right\} \\ &= \sigma^2 N(P-L-2) \end{aligned}$$

The noise covariance matrix may then be computed.

$$\begin{aligned} R_n &= \frac{1}{N}E\left[\tilde{\Theta}\tilde{\Theta}^t\right] \\ &= \frac{1}{N}(A^tA)^{-1}A^tE\left[\nu\nu^t\right]A(A^tA)^{-1} \\ &= \sigma^2(A^tA)^{-1}A^tA(A^tA)^{-1} \\ &= E\left[tr\{\epsilon\epsilon^t\}\right](A^tA)^{-1}/(N(P-L-2)) \\ &= E\left[\hat{R}_n\right] \end{aligned}$$

where $\hat{R}_n$ is given in (2.12).

A.2 Derivation of whitening matrix

The corrected noise covariance matrix after subspace processing is denoted as $\bar{R}_n$ where

$$\bar{R}_n = \hat{U}_s^t \hat{R}_n \hat{U}_s \ . \tag{A.1}$$

The whitening filter matrix W has the property that $\bar{R}_n^{-1} = WW^t$. Let $\bar{R}_n = U_n S_n V_n^t$ be the singular value decomposition where S_n is a diagonal matrix of singular values. Then the whitening matrix is is given by

$$W = V_n \left[\sqrt{S_n}\right]^{-1} \tag{A.2}$$

and the whitened feature vectors are given by $Y = W\hat{Y}$.

A.3 Expectation-maximization algorithm

A.3.1 Expectation step

The Q function used in the EM algorithm is defined as the expectation of the joint log-likelihood function given the current estimates of the parameters. Knowing this, we can write

$$\begin{aligned} & Q(K, E_K, \Pi_K; E_K^{(i)}, \Pi_K^{(i)}) \\ = \ & E_{x|y}[\log p_{y,x}(y, X|E_K, \Pi_K, \hat{\alpha})|y, K, E_K^{(i)}, \Pi_K^{(i)}, \hat{\alpha}] \qquad \text{(A.3)} \\ = \ & \sum_{k=1}^{K} \left[\log p_{y|x}(y|k, E_K, \Pi_K, \hat{\alpha}) \log p_x(k|\Pi_K)\right] p_{x|y}(k|y, E_K^{(i)}, \Pi_K^{(i)}, \hat{\alpha}). \qquad \text{(A.4)} \end{aligned}$$

Because of conditional independence, the one-to-one mapping of $x_n \rightarrow y_n$, and $p_x(k|\Pi_K) = \pi_k$,

$$\begin{aligned} & Q(K, E_K, \Pi_K; E_K^{(i)}, \Pi_K^{(i)}) \\ = \ & \sum_{k=1}^{K} \left\{ \sum_{n=1}^{N} \left[-\frac{1}{2} \left(y_n^t y_n - e_k^t y_n y_n^t e_k \right) p_{x_n|y_n}(k|y_n, E_K^{(i)}, \Pi_K^{(i)}, \hat{\alpha}) \right] \right. \\ & \left. -\frac{M-1}{2} \log(2\pi) \sum_{n=1}^{N} p_{x_n|y_n}(k|y_n, E_K^{(i)}, \Pi_K^{(i)}, \hat{\alpha}) + \right. \end{aligned}$$

$$\log \pi_k \sum_{n=1}^{N} p_{x_n|y_n}(k|y_n, E_K^{(i)}, \Pi_K^{(i)}, \hat{\alpha}) \Bigg\} \tag{A.5}$$

Now define

$$\bar{N}_{k|K}^{(i)} = \sum_{n=1}^{N} p_{x_n|y_n}(k|y_n, E_K^{(i)}, \Pi_K^{(i)}, \hat{\alpha}) \tag{A.6}$$

and

$$\bar{R}_{k|K}^{(i)} = \frac{1}{\bar{N}_{k|K}} \sum_{n=1}^{N} y_n y_n^t p_{x_n|y_n}(k|y_n, E_K^{(i)}, \Pi_K^{(i)}, \hat{\alpha}) \tag{A.7}$$

We can then write the Q function in its final form.

$$\begin{aligned} & Q(K, E_K, \Pi_K; E_K^{(i)}, \Pi_K^{(i)}) \\ = & \sum_{k=1}^{K} \bar{N}_{k|K}^{(i)} \left\{ -\frac{1}{2} tr(\bar{R}_{k|K}^{(i)}) + \frac{1}{2} e_k^t \bar{R}_{k|K}^{(i)} e_k - \frac{M-1}{2} \log(2\pi) + \log \pi_k \right\} \end{aligned} \tag{A.8}$$

A.3.2 Maximization step

In order to find $E^{(i+1)}$, we maximize Q with respect to each $e_k, k \in \{1, 2, ..., K\}$. We can see that all the terms are constant with respect to e_k except $\frac{1}{2} e_k^t \bar{R}_{k|K}^{(i)} e_k$. So maximizing this factor with respect to e_k is equivalent to maximizing Q. So the update equation becomes

$$e_k^{(i+1)} = \underset{e_k}{\operatorname{argmax}} \left(e_k^t \bar{R}_{k|K}^{(i)} e_k \right) \tag{A.9}$$

It is known from linear algebra theory that the solution to this maximization is the principle eigenvector of $\bar{R}_{k|K}^{(i)}$. If we let $e_{max}(R)$ be the principle eigenvector of R, we can write the update equation as

$$e_k^{(i+1)} = e_{max}(\bar{R}_{k|K}^{(i)}) \tag{A.10}$$

Now we need to find $\Pi_K^{(i+1)}$. We can see that all the terms of Q are constant with respect to each π_k except for $\bar{N}_{k|K}^{(i)} \log \pi_k$. Therefore, maximizing this term w.r.t π_k is equivalent to maximizing Q w.r.t. π_k. The problem is a constrained optimization because $\sum_{k=1}^{K} \pi_k = 1$ due to the fact that these are probabilities. If method of

Lagrange multipliers is applied, we find that the update equations for ${\Pi_K}^{(i+1)}$ is the following equation.

$$\pi_k^{(i+1)} = \frac{\bar{N}_{k|K}^{(i)}}{N} \tag{A.11}$$

A.4 Derivation of cluster merging

In this section, we derive the distance function used for cluster merging in minimization of the MDL criterion. Let l and m denote the indices of the two clusters to be merged. Let E_K and Π_K to be the result of running the EM algorithm to convergence with clusters of order K, and let $E_{(l,m)|K}$ and $\Pi_{(l,m)|K}$ denote new parameter sets in which the parameters for clusters l and m are equated. This means that $\Pi_{(l,m)|K} = \Pi_K$ and $E_{(l,m)|K}$ remains the same except for the column vectors corresponding to the clusters l and m which are modified to be

$$e_l \;=\; e_m = e_{(l,m)} \tag{A.12}$$

where $e_{(l,m)}$ denotes the common value of the parameter vectors.

Also define the subscript $E_{(l,m)|K-1}$ and $\Pi_{(l,m)|K-1}$ to be parameter sets with $K-1$ clusters in which the l and m clusters have been merged into a single cluster with parameters $e_{(l,m)}$ and $\pi_{(l,m)} = \pi_l + \pi_m$. The change in the MDL criterion produced by merging the clusters l and m is then given by

$$\begin{aligned} & MDL(K-1, E_{(l,m)|K-1}, \Pi_{(l,m)|K-1}) - MDL(K, E_K, \Pi_K) \\ = \;& MDL(K-1, E_{(l,m)|K-1}, \Pi_{(l,m)|K-1}) - MDL(K, E_{(l,m)|K}, \Pi_{(l,m)|K}) \\ & + MDL(K, E_{(l,m)|K}, \Pi_{(l,m)|K}) - MDL(K, E_K, \Pi_K) \end{aligned} \tag{A.13}$$

From (2.33), we can see that

$$MDL(K-1, E_{(l,m)|K-1}, \Pi_{(l,m)|K-1}) - MDL(K, E_{(l,m)|K}, \Pi_{(l,m)|K}) = -\frac{M}{2}\log(NM)\ ; \tag{A.14}$$

and from the upper bounding properties of the Q-function, we know that

$$MDL(K, E_{(l,m)|K}, \Pi_{(l,m)|K}) - MDL(K, E_K, \Pi_K)$$

$$\leq \quad Q(K, E_K, \Pi_K; E_K, \Pi_K) - Q(K, E_{(l,m)|K}, \Pi_{(l,m)|K}; E_K, \Pi_K) \ . \qquad \text{(A.15)}$$

Substituting into (A.13) results in the following inequality.

$$\begin{aligned} & MDL(K-1, E_{(l,m)|K-1}, \Pi_{(l,m)|K-1}) - MDL(K, E_K, \Pi_K) \\ \leq \quad & Q(K, E_K, \Pi_K; E_K, \Pi_K) - Q(K, E_{(l,m)|K}, \Pi_{(l,m)|K}; E_K, \Pi_K) - \frac{M}{2}\log(NM) \end{aligned} \qquad \text{(A.16)}$$

Since we assume that E_K and Π_K are the result of running the EM algorithm to convergence, we know that

$$(E_K, \Pi_K) \quad = \quad \arg\max_{E'_K, \Pi'_K} Q(K, E'_K, \Pi'_K; E_K, \Pi_K) \ . \qquad \text{(A.17)}$$

Furthermore, the inequality of (A.13) is most tight when $E_{(l,m)|K}$ and $\Pi_{(l,m)|K}$ are chosen to be

$$(\hat{E}_{(l,m)|K}, \hat{\Pi}_{(l,m)|K}) \quad = \arg\max_{E'_{(l,m)|K}, \Pi'_{(l,m)|K}} Q(K, E'_{(l,m)|K}, \Pi'_{(l,m)|K}; E_K, \Pi_K) \ . \qquad \text{(A.18)}$$

The optimization of (A.18) is a constrained version of (A.17). So it is easily shown that values of $(\hat{E}_{(l,m)|K}, \hat{\Pi}_{(l,m)|K})$ and (E_K, Π_K) are equal except for the parameter vector $e_{(l,m)}$ which is given by

$$e_{(l,m)} = e_{max}\{\bar{R}_{l|K} + \bar{R}_{m|K}\}, \qquad \text{(A.19)}$$

where $e_{max}\{R\}$ is the principle eigenvector of R, and $\bar{R}_{l|K}$ and $\bar{R}_{m|K}$ are computed using (2.30).

Substituting into (A.16) and simplifying the expression for the Q function results in

$$\begin{aligned} & MDL(K-1, E_{(l,m)|K-1}, \Pi_{(l,m)|K-1}) - MDL(K, E_K, \Pi_K) \\ \leq \quad & Q(K, E_K, \Pi_K; E_K, \Pi_K) - Q(K, \hat{E}_{(l,m)|K}, \hat{\Pi}_{(l,m)|K}; E_K, \Pi_K) - \frac{M}{2}\log(NM) \\ = \quad & \sigma_{max}(\bar{R}_{l|K}) + \sigma_{max}(\bar{R}_{m|K}) - \sigma_{max}(\bar{R}_{l|K} + \bar{R}_{m|K}) - \frac{M}{2}\log(NM) \end{aligned} \qquad \text{(A.20)}$$

which produces the final result

$$MDL(K-1, E_{(l,m)|K}, \Pi_{(l,m)|K}) - MDL(K, E_K, \Pi_K) \leq d(l,m) - \frac{M}{2}\log(NM) \qquad \text{(A.21)}$$

where $d(l,m)$ is the positive distance function of (2.34).

APPENDIX B
DERIVATIONS FOR SUPERTEMPORAL RESOLUTION ANALYSIS

B.1 Details of nuisance parameter removal

We have defined $\mathbf{P}$ to be an $m \times m$ projection matrix constructed so that $\mathbf{P}\psi_n = 0$, and the other eigenvalues are equal to one. The matrix is used to remove the nuisance parameters from the data,

$$\mathbf{P}y_n = \alpha_n \mathbf{P}\mathbf{A}_n e + \mathbf{P}\omega_n \tag{B.1}$$

However, since the density function of $\mathbf{P}y_n$ is singular and $\mathbf{P}\omega_n$ is not white, we will instead model the density function of $\mathbf{V}y_n$, where $\mathbf{V}$ is an $(m-2) \times m$ orthonormal matrix derived from $\mathbf{P}$. Two degrees of freedom are reduced by $\mathbf{P}$. $\mathbf{V}$ is found by taking the singular value decomposition of $\mathbf{P}$.

$$\mathbf{P} = \mathbf{U}^T \Sigma \mathbf{V} \tag{B.2}$$

since it is known that the eigenvalues of $\mathbf{P}$ are one or zero, $\Sigma = \mathbf{I}$. Therefore, $\mathbf{P} = \mathbf{U}^T\mathbf{V}$. Note that $\mathbf{V}$ has the same nullspace as $\mathbf{P}$ and therefore $\mathbf{V}\psi_n = 0$. The modified model becomes

$$\mathbf{V}y_n = \mathbf{V}\mathbf{A}_n e\alpha_n + \mathbf{V}\omega_n \tag{B.3}$$

Because $\mathbf{V}\omega_n$ is still white, we now form the likelihood function for each modified pixel.

$$p(\mathbf{V}y_n | e, \alpha_n) = \frac{1}{(2\pi)^{\frac{m-k}{2}}} \exp\left(-\frac{1}{2}\left\|\mathbf{V}y_n - \mathbf{V}\mathbf{A}_n e\alpha_n\right\|^2\right) \tag{B.4}$$

However, since $\mathbf{U}$ is orthonormal, it is easy to see that

$$\left\|\mathbf{V}y_n - \mathbf{V}\tilde{\mathbf{A}}_n e\alpha_n\right\| \tag{B.5}$$

$$= \left\|\mathbf{U}^T(\mathbf{V}y_n - \mathbf{V}\tilde{\mathbf{A}}_n e\alpha_n)\right\| \tag{B.6}$$

$$= \left\|\mathbf{U}^T\mathbf{V}y_n - \mathbf{U}^T\mathbf{V}\tilde{\mathbf{A}}_n e\alpha_n)\right\| \tag{B.7}$$

$$= \|\mathbf{P}y_n - \mathbf{P}\mathbf{A}_n e\alpha_n)\| \tag{B.8}$$

Now define $\check{y}_n = \mathbf{V}y_n$, $\tilde{y}_n = \mathbf{P}y_n$, and $\tilde{\mathbf{A}}_n = \mathbf{P}\mathbf{A}_n$,

$$p(\check{y}_n|e,\alpha_n) = \frac{1}{(2\pi)^{\frac{m-k}{2}}}\exp\left(-\frac{1}{2}\left\|\tilde{y}_n - \tilde{\mathbf{A}}_n e\alpha_n\right\|^2\right) \tag{B.9}$$

B.2 Balloon model

The synthetic BOLD signal used in our data simulator is based upon the balloon model developed by Buxton, *et. al.* [8]. This model of the BOLD signal is based upon the assumption that the venous compartment is an elastic balloon. Therefore, the volume of the compartment expands and contracts with transient differences between blood inflow and outflow. In the subsequent discussion, the values for blood inflow f_{out}, blood outflow f_{in}, volume v, and deoxyhemoglobin concentration q have been normalized by their resting state values and are unitless.

We first define the transient relationship between the normalized outflow f_{out} and the normalized volume v using an empirical equation describing the elasticity of the balloon. The unitless constants a, b, and c are found in Table B.1.

$$f_{out}(v) = ae^{b(v-1)} + (1-a) \tag{B.10}$$

The nonlinear form of this equation describes a relationship where at low volumes, large changes in volume lead to small changes in outflow. At high volumes, small changes in volume lead to large changes in outflow.

We then use the system of equations developed in [8] (Equations B.11, B.12, B.13, and B.14) to generate the synthetic BOLD response signal.

First, the differential equation describing the change in volume of the venous compartment due to changes in the difference between inflow and outflow is expressed.

Table B.1
Constants used in balloon model

Constant	Value	Constant	Value
V_0	0.04	k_3	$2E_0 - 0.2$
E_0	0.01	τ_0	1.0 s
k_1	$7E_0$	a	0.02
k_2	2.0	b	12.0

The value τ_0 is the mean transit time through the venous compartment and given in Table B.1 in seconds.

$$\frac{dv(t)}{dt} = \frac{1}{\tau_0}[f_{in}(t) - f_{out}(v(t))] \tag{B.11}$$

Equation B.10 was substituted into Equation B.11, and the resulting expression was numerically integrated to find the normalized time evolution of volume $v(t)$. We find the normalized blood outflow time evolution $f_{out}(t)$. by substituting the resulting $v(t)$ back into Equation B.10,

Extraction fraction E, which is the amount of oxygen removed from the blood by neuronal metabolism, is defined as

$$E(t) = 1 - (1 - E_0)^{1/f_{in}(t)} \tag{B.12}$$

where the unitless E_0 is the resting state extraction fraction and is found in Table B.1.

The change in deoxyhemoglobin concentration can be expressed as a differential equation describing the interplay between normalized flow, volume, and extraction fraction.

$$\frac{dq(t)}{dt} = \frac{1}{\tau_0}\left[f_{in}(t)\frac{E(t)}{E_0} - f_{out}(v(t))\frac{q(t)}{v(t)}\right] \tag{B.13}$$

The time evolution of the normalized deoxyhemoglobin concentration $q(t)$ was then found by substituting Equation B.12 into Equation B.13 and numerically integrating. The BOLD signal was then found using the equation

$$S_{BOLD} = V_0\left[k_1(1 - q(t)) + k_2\left(1 - \frac{q(t)}{v(t)}\right) + k_3(1 - v(t))\right], \tag{B.14}$$

where k_1, k_2, and k_3 are unitless constants and V_0 is the resting volume fraction of the venous compartment (see Table B.1). The first term represents inherent extravascular compartment signal changes, the second represents inherent intravascular compartment changes, and the third represents changes due to transport between the two compartments. The BOLD signal generated is given in Figure 3.2.

VITA

VITA

Sea Chen was born on April 28, 1976 in Taipei, Taiwan. When he was one, he moved to Louisville, KY, but spent most of his childhood in Munster, IN. He started college at Purdue University at West Lafayette, IN, and in 1994 and graduated with a B.S. degree in Electrical Engineering in 1997. In 1997, he entered combined M.D./Ph.D program at Indiana University School of Medicine in Indianapolis and in the newly formed Department of Biomedical Engineering at Purdue University. He completed his first 2 pre-clinical medical school years in 1999 and commenced his Ph.D. training thereafter.